SCANNING TUNNELING MICROSCOPY STUDIES OF CLUSTER DIFFUSION IN A HIGHLY MISMATCHED SYSTEM: COPPER ON SILVER(111)

BY

ANDREW W. SIGNOR

DISSERTATION

Submitted in partial fulfillment of the requirements
for the degree of Doctor of Philosophy in Materials Science and Engineering
in the Graduate College of the
University of Illinois at Urbana-Champaign, 2010

Urbana, Illinois

Doctoral Committee:

Professor John H. Weaver, Chair
Professor Dallas R. Trinkle
Professor Joseph W. Lyding
Professor Gert Ehrlich

ABSTRACT

I have used low-temperature scanning tunneling microscopy to investigate cluster diffusion phenomena in both the early stages of nucleation and growth and the late stages for a highly mismatched system, Cu on Ag(111). In particular, activation energies and prefactors for cluster diffusion are measured directly by tracking cluster motion with atomic precision at multiple temperatures to determine the temperature dependence of hop rates. In contrast with larger homoepitaxial islands on Ag(111) and Cu(111), small-to-medium sized clusters (3-30 atoms) of Cu on Ag(111) display a non-monotonic size dependence of the diffusion barrier, with surprisingly low diffusion barriers for clusters containing up to ~26 atoms. Molecular dynamics simulations reveal a novel dislocation-mediated island diffusion mechanism and predict barriers that are in very good agreement with experiment. In this mechanism, the barrier to nucleate a dislocation, and hence diffuse, is sensitive to island size and shape. Experimental studies of the early stages of nucleation and growth of Cu on Ag(111) reveal that trimers, once formed, have significantly higher mobilities than either atoms or dimers. While transient, this mobility makes trimers the dominant contributor to mass transport at temperatures allowing trimer formation ($T \geq 24$ K). Using the STM tip, we constructed linear and compact trimers at 5 K and investigated their stabilities and diffusion parameters as a function of temperature. Analysis shows that the diffusion barrier for linear trimers is very low, 13.6 meV, compared to 65 meV for atoms, while the compact trimer is stable and immobile. The details of trimer diffusion and rotation provide insights into the intermediate diffusion steps and indicate that the large lattice mismatch plays an important role. The properties of Cu trimers on Ag(111) contrast with those reported for homoepitaxial trimers on

fcc(111) surfaces. Because the diffusion phenomena for Cu trimers and other clusters on Ag(111) are largely a result of lattice mismatch, similar phenomena may exist in the early stages of nucleation and growth of other heteroepitaxial systems.

To my parents, William E. and Brenda M. Signor, who encouraged my interest in science at a young age, and to Thomas and Mildred Doughty, whose generosity will always be remembered.

ACKNOWLEDGEMENTS

First, I would like to thank my thesis advisor, Prof. John H. Weaver for his guidance, support, and personal friendship throughout my years at the University of Illinois. Our morning conversations over coffee and fruit and our time together on the range will especially be missed. I would also like to acknowledge the tremendous experimental mentorship of Koji S. Nakayama, who taught me the art and science of scanning tunneling microscopy.

I am extremely grateful for the collaboration with Henry H. Wu and Dallas R. Trinkle, whose theory and simulations added a level of depth and detailed understanding to this work that would have been unattainable through experiment alone.

The computer programming expertise of J.S. Palmer helped very much in developing the data analysis routines used in this work. I also thank R. E. Butera, P. Swaminathan, C. M. Aldao, J. W. Lyding, and G. Ehrlich for many stimulating discussions.

This work was supported by the National Science Foundation under Grant No. DMR 0703995.

TABLE OF CONTENTS

CHAPTER 1

SYNOPSIS

1.1 Background and Motivation

Surface diffusion of atoms and clusters has been studied for decades, driven in large part by their important role in the technologically important thin film and crystal growth processes. The advent of field ion microscopy and, later, scanning tunneling microscopy (STM), allowed the imaging of individual atoms on surfaces, enabling diffusion of atoms and clusters to be observed directly. Direct observation of atom and cluster diffusion has revealed a diversity of surface diffusion phenomena and has lead to the discovery of many interesting and unexpected mechanisms [1-3]. This is especially true for cluster diffusion, because of the numerous ways a collection of atoms can move on a surface. Despite predictions of interesting diffusion phenomena resulting from lattice mismatch [4, 5], relatively little work has been done in heteroepitaxial systems with a large lattice mismatch.

The aim of my research is to investigate cluster diffusion processes in a system with a large lattice mismatch. I chose Cu on Ag(111) as a model system because of the large mismatch (~12%, a_{Ag}=4.09 Å, a_{Cu}=3.61 Å) and because it is an immiscible system where complications due to reaction and intermixing can be avoided. Furthermore, homoepitaxial island diffusion on Ag(111) and Cu(111) [6] and Cu atom and dimer diffusion on Ag(111) [7] have been extensively studied, providing a well-developed backdrop against which to contrast my findings. The existence of reliable embedded atom potentials for Cu and Ag also allows for molecular dynamics simulations to

compliment the experimental measurements and provide details regarding atomic scale mechanisms that are inaccessible to experiment.

My research was motivated by initial observations with STM that showed rapid, low-temperature diffusion of medium sized clusters of Cu on Ag(111), while smaller and larger clusters had limited or no mobility. These preliminary results are represented by the STM images of Fig. 1.1, which were selected from a data set containing >300 images collected at 130 K. The highlighted ~15-20 atom cluster underwent significant diffusion, while the smaller and larger islands shown had limited or no mobility. Also, diffusion occurred with no apparent change in shape or size. These observations were interesting, because homoepitaxial islands on the (111) and other facets of Ag and Cu migrate through edge diffusion or adatom evaporation/condensation at the edges—mechanisms which are precluded by the lack of change in size or shape for Cu islands on Ag(111). Furthermore, these mechanisms result in a diffusivity that is a smoothly decreasing function of island size. Instead of a diffusivity that smoothly varies with island size, Fig. 1.1 suggests a "magic size" effect similar to that predicted by Hamilton for highly mismatched heteroepitaxial island diffusion. Hamilton proposed that island diffusion can occur through the nucleation and glide of misfit dislocations, and islands of a special size favoring dislocation nucleation had a reduced barrier for motion. My experimental research, coupled with molecular dynamics simulations performed by Henry Wu and Dallas Trinkle, show that a dislocation mechanism similar to that proposed by Hamilton can explain the unique diffusion phenomena for Cu clusters on Ag(111).

1.2 Overview

Chapter 2 outlines the experimental setup used and modifications that were made to enable improvements and better controlled experiments than those that provided the preliminary results. The improved experimental setup allowed Cu atoms to be deposited onto the Ag(111) substrate which was held at 5 K on the STM stage. This allowed precise knowledge of the adatom density, and it enabled the early stages of nucleation and growth to be observed *in situ.*

Chapter 3 presents experimental measurements, combined with molecular dynamics simulations of the diffusion of Cu islands on Ag(111) spanning a size range of 4-26 atoms. The experimental findings show that, just as in the preliminary results of Fig. 1.1, diffusion occurs without changes in shape or size. Trajectories reveal that, for all mobile clusters, hopping occurs among a discrete set of adsorption sites separated by the Ag(111) nearest-neighbor fcc sites. These qualitative observations preclude individual atom diffusion events, such as edge diffusion or evaporation/condensation at cluster edges, because these processes would cause fluctuations in size and/or shape and would not explain the observed displacements. The same ensemble of clusters was tracked at multiple temperatures between 80-90 K and the temperature dependence of the hop rates allow the diffusion barriers and prefactors to be determined directly from experiment. Surprisingly, clusters as large as ~26 atoms have diffusion barriers as low as ~250 meV, compared to a diffusion barrier of ~500 meV for homoepitaxial island diffusion on either Cu(111) or Ag(111). In contrast to Hamilton's prediction of a singular "magic size" with a low diffusion barrier, my experimental measurements reveal multiple sizes with low diffusion barriers.

The molecular dynamics simulations reveal, in atomic-level detail, a dislocation mechanism allowing low diffusion barriers for islands of the proper size and shape. In this mechanism, a metastable stacking fault is formed, with a portion of the atoms in fcc sites, and the rest in hcp sites. Because the lattice constant of Cu is smaller than that of Ag, the Burger's vector of the dislocation is such that Cu-Cu bond lengths are shortened, relieving strain. This mechanism provides a low-barrier pathway for diffusion for islands with shapes that allow dislocation formation without breaking Cu-Cu bonds, but does not occur for islands with closed-shell structures that would require bond breaking. This means that, besides island size, shape is extremely important in determining the diffusion barrier. In agreement with the experiments, the MD simulations predict multiple "magic sizes", and the predicted diffusion barriers are in excellent agreement with experiment. The diffusion barriers for island sizes and shapes favoring this mechanism are lower than that for edge diffusion or Ostwald ripening, and cluster coalescence is the kinetically preferred coarsening pathway. This work shows that dislocations in highly-mismatched heteroepitaxial islands reduce barriers for islands of special sizes and shapes in the same way that they reduce the yield stress of bulk materials: by enabling slip to occur in a piecewise fashion.

The work presented in Chapter 3 shows that lattice mismatch plays an important role in heteroepitaxial island diffusion, promoting a low-barrier misfit-dislocation mechanism and that island shape plays a significant role. While this work establishes that an island with a non-equilibrium shape may have significantly lower diffusion barrier than the ground-state configuration, it does not show whether non-equilibrium shapes would persist long enough for significant diffusion to occur.

The work presented in Chapter 4 investigates the stability and diffusion of a non-equilibrium structure, a linear trimer chain, and compares them to those of the ground-state compact configuration. In an STM study of the early stages of nucleation and growth of Cu on Ag(111), it is observed that trimer nucleation results in a cluster with significantly higher mobility than either individual atoms or dimers upon their formation. The high trimer mobility is transient, existing only for a short time after trimer formation at 24 K, yet the significant displacements attained make the trimer an important contributor to mass transport. Subsequent the transient mobility events, the trimers are compact and immobile, consistent with MD simulations that predict a high diffusion barrier for the ground-state compact trimer. The trimer nucleation and migration measurements conducted at 24 K suggest that atom-dimer combination results in a very mobile precursor to the immobile, compact trimers; however, from these data alone, one cannot conclude much regarding the nature of the precursor—only the initial and final locations are known, and motion is too fast and too short lived to be studied directly at temperatures where they form naturally on experimental time scales. It is proposed that a non-equilibrium-shaped trimer may have a very low diffusion barrier and act as a highly mobile precursor to the immobile compact trimer. Using the STM tip to manipulate atoms, linear chain and compact trimers are constructed at 5 K, and their stability and diffusion properties are investigated. It is shown that the linear trimer chain has an extremely low diffusion barrier, 13.6 meV, compared to 65 meV for atoms, while the compact trimer is very stable and immobile. Based on these results, it is proposed that the linear chain acts as a very mobile precursor to the relatively immobile compact trimer and is responsible for the large displacements observed upon nucleation at elevated

temperatures. The trimer chain undergoes length-wise hopping along the close-packed <110>, as well as rotation about an end atom. The details of trimer chain diffusion and rotation provide insight into the intermediate diffusion steps and indicate that the large lattice mismatch plays an important role in the diffusion properties of the trimer chain in the same way it does for larger Cu clusters on Ag(111). Because the diffusion phenomena for Cu trimers and other clusters on Ag(111) are largely a result of lattice mismatch, similar phenomena may exist in the early stages of nucleation and growth of other heteroepitaxial systems.

1.3 References

1. G. Ehrlich, *Surf. Sci.* **246**, 1 (1991).
2. T. T. Tsong, *Rep. Prog. Phys.* **51**, 759 (1988).
3. A. G. Naumovets, Z. Y. Zhang, *Surf. Sci.* **500**, 414 (2002).
4. . C. Hamilton, M. S. Daw, and S. M. Foiles, Phys. Rev. Lett. **74**, 2760 (1995).
5. J. C. Hamilton, M. S. Daw, and S. M. Foiles, Phys. Rev. Lett. **74**, 2760 (1995).
6. D. C. Schlößer et al., Surf. Sci. **465** 19 (2000).
7. K. Morgenstern, K.-F. Braun, K.-H. Rieder, Phys. Rev. Lett. **93** 056102 (2004).

1.4 Figures

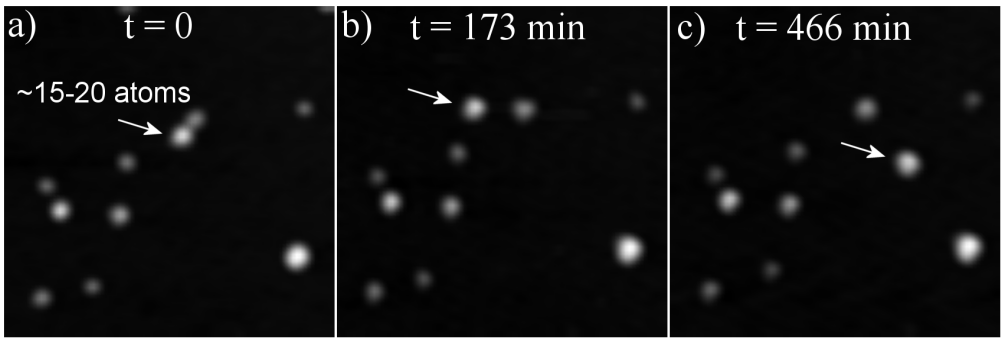

Figure 1.1 Anomalous diffusion of Cu cluster on Ag(111) at 130 K. The 15-20 atom cluster indicated underwent significant diffusion while smaller and larger clusters were completely immobile. Cluster diffusion occurred in the absence of shape changes or atom exchange between clusters, in contrast to homoepitaxial island diffusion on Ag(111) or Cu(111).

CHAPTER 2

EXPERIMENTAL PROCEDURES

2.1 Microscope

My experimental measurements of cluster formation and diffusion were conducted in an Omicron low-temperature scanning tunneling microscope with the capability of imaging between 5 K and 300 K. In this microscope design, the stage is cooled by bringing it into contact with a cryostat that is filled with either liquid He or liquid N_2, depending on the desired experimental temperature. Once the sample is cooled to the base temperature (either 5 K or 78 K), the stage is then disconnected from the cryostat to mechanically isolate the stage and engage the vibration damping system. A metal shroud, which was permanently attached to the cryostat, surrounded the entire stage assembly to prevent heating of the stage and sample from ambient radiation. Besides maintaining the low temperatures, this metal shroud also acted as a cryopump, allowing the sample surface to remain clean for the long time periods over which the measurements were performed.

The sample temperature was measured with a silicon diode in direct contact with the back of the sample holder. A Lakeshore temperature controller regulated the power to a resistor within the stage, allowing a sample temperature range between 5 K and 300 K. The cryogen reservoir, when full, allowed continuous cooling for 10-24 hours, depending on the sample temperature. If an experiment required cooling for longer periods, the measurement was paused, the tip was retracted a small amount, and the cryostat was refilled. Retracting the tip only a small amount during the refill process

allowed for the same experimental surface region, to be imaged subsequent the refill. This enabled experimental measurements of the same clusters to be performed indefinitely (sometimes several weeks), allowing a sufficient number of diffusion events to be observed for good statistics.

2.2 Sample Preparation and Experimental Setup

The Ag(111) substrates were thick films (100's of monolayers) grown in a preparation chamber (base pressure ~4×10^{-11} Torr) by evaporating Ag onto Si(111)-7×7 cooled to ~20 K with a helium refrigerator, followed by an anneal at ~600 K for a few seconds. These films have large (~10^4 nm^2), flat regions free of defects or steps [1], making them ideal for diffusion studies. The excellent agreement between our measurements of Cu atom and dimer diffusion barriers with those measured on Ag(111) single crystals [2] indicate a high quality surface. This also provides a confirmation of temperature accuracy.

In preliminary experiments, Cu was also deposited in the preparation chamber. This was done in a similar manner to the Ag film deposition, with the freshly prepared Ag substrate was cooled to ~20 K with a helium refrigerator, and Cu was deposited. The Cu flux was monitored with a quartz crystal microbalance, and once the desired amount was deposited, the sample was then transferred, as quickly as possible, to the cooled STM stage. Figure 2.1 is a schematic of the setup used in this process. While this setup allowed for the preliminary results motivating further work, it was not ideal. It required transferring the cold sample with room-temperature manipulators to the STM stage. During this process, which took 2-4 minutes, the sample warmed to an unknown

temperature ~ 100-200 K at which a significant and uncontrollable amount of atom and cluster diffusion occurred before the surface could be imaged. Besides preventing any observation of the early stages of nucleation and growth, this also made determination of island sizes difficult, as the Cu adatom density was not precisely known.

This experimental setup was significantly improved upon by installing a homebuilt evaporator onto the measurement chamber. This setup, illustrated in Fig. 2.2, enabled deposition of dilute amounts of Cu while the sample was on the STM stage at 5 K, a temperature where atom and cluster diffusion does not occur. The Cu source was heated in a W basket, and water cooling minimized outgasing from the evaporator walls. During evaporation, the pressure remained ~ 5×10^{-11} Torr. A small aperture created a narrow beam, protecting the critical components of the microscope and limiting exposure to the sample surface. A quartz crystal microbalance mounted in the evaporator was used to monitor the flux, and it was calibrated by counting individual atoms in STM images collected at 5 K immediately after exposure. This, combined with a shutter, allowed for precise control of the amount of Cu, allowed precise knowledge of the adatom density, and it enabled the early stages of nucleation and growth to be observed *in situ* as the sample was warmed from 5 K. This is illustrated in Fig. 2.3, showing the evolution from individual Cu atoms at 5 K (a) to clusters at elevated temperature (b). With this setup, both cluster formation at T ~20 K and cluster diffusion at elevated temperatures can be followed. Figure 2.3 (c) shows a temperature-time plot for an experiment where individual atoms were deposited and imaged at 5 K, followed by cluster formation at elevated temperature, and cluster diffusion measurements in the 80-90 K temperature range.

2.3 Particle Tracking

For quantitative diffusion measurements, the trajectories of particles must be extracted from sets of, in some cases, thousands of images. In order to do this, a set of particle-tracking programs for Matlab, initially developed for tracking colloidal particles in solution with optical microscopy [3], were adapted for STM. These programs identifiy all particles (bright features on a dark background) in an image and determine their centers of mass (see program "Mattrack" in the Appendix), correlate their x,y coordinates between successive image frames so that the trajectory of each individual particle can be extracted, and use the trajectories of "immobile" particles as a reference to correct for thermal drift of the microscope and to convert pixel values to calibrated distances (see program "Traj" in the Appendix). Besides making data analysis more efficient and systematic, these programs enabled trajectories with atomic precision to be determined, even without atomic-level contrast in the STM images.

2.4 References

1. K. Morgenstern, K.-F. Braun, K.-H. Rieder, Phys. Rev. Lett. **93** 056102 (2004).
2. L. Huang, S. J. Chey, J. H. Weaver, Surf. Sci. **416** L1101 (1998).
3. J. C. Crocker and D. G. Grier, J. Colloid Interface Sci. **179**, 298 (1996).

2.5 Figures

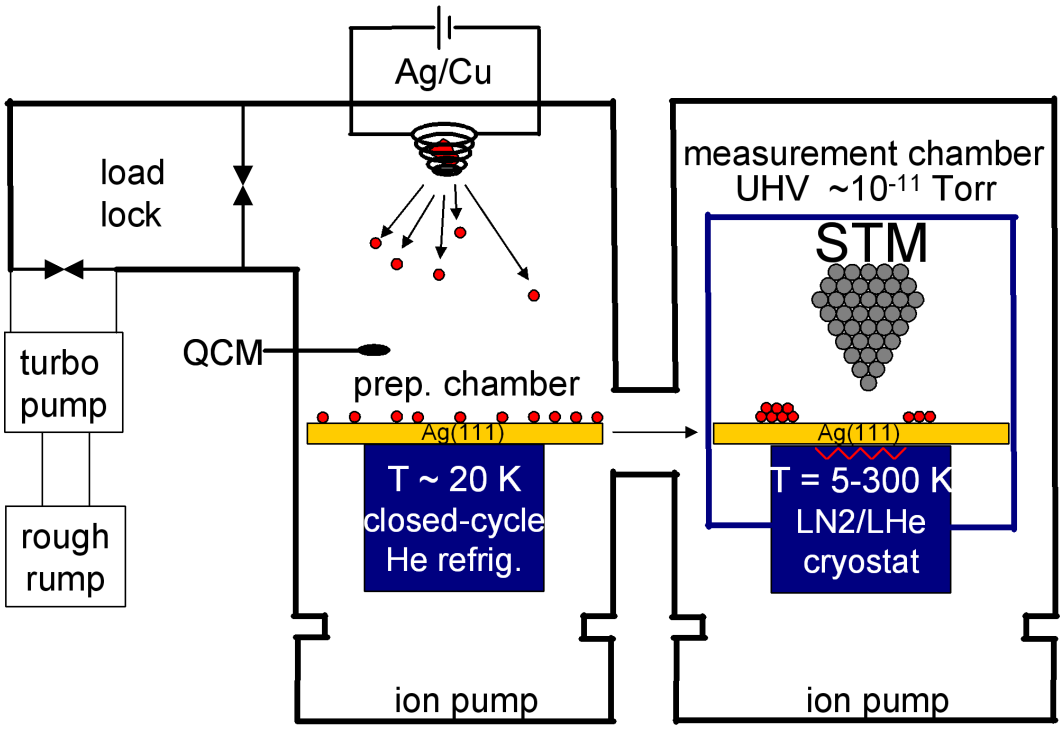

Figure 2.1 Initial experimental setup. Both substrate preparation and Cu deposition occur in the prep. chamber, with the sample cooled to ~20 K with a He refrigerator. This setup required the sample to then be transferred via a room-temperature manipulator to the cooled STM stage. During this transfer, the sample warmed to ~100-200 K, allowing significant and uncontrollable amounts of atom and cluster diffusion prior to imaging.

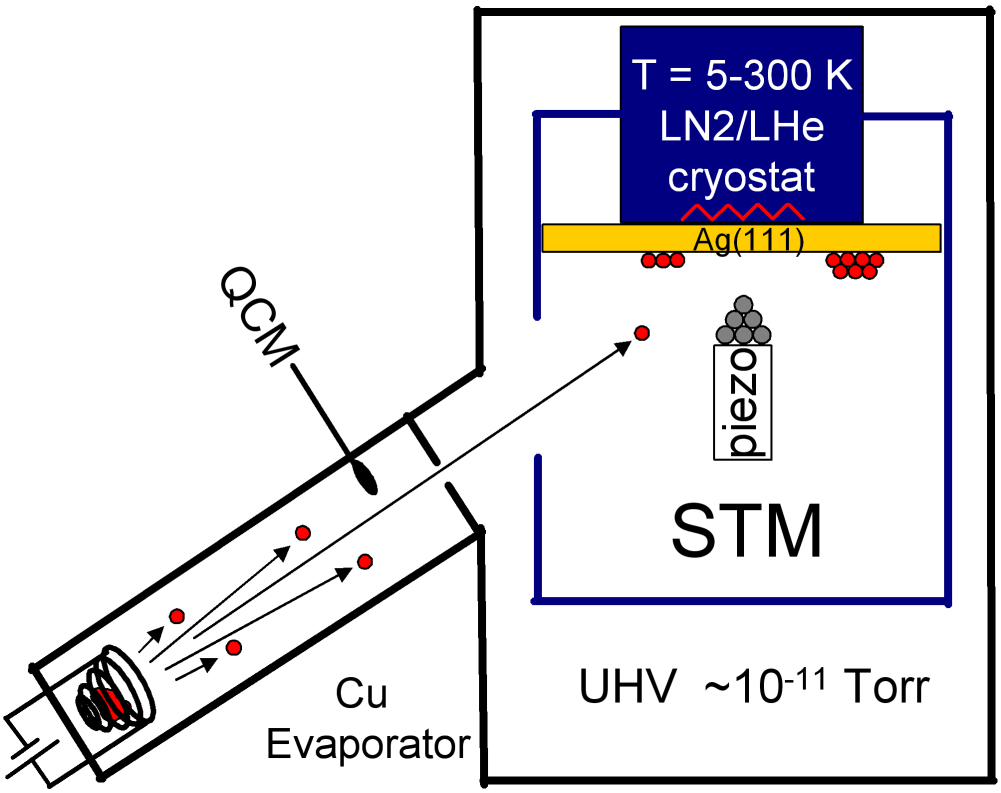

Figure 2.2 Improved experimental setup, incorporating a homebuilt Cu evaporator onto the STM chamber. Cu flux was monitored with a quartz crystal microbalance (QCM), and exposure was limited to the sample stage by a small aperture which prevented contamination of microscope components. This setup allowed Cu deposition with the sample on the STM stage, where the temperature could be very well controlled, and the early stages of nucleation and growth could be observed.

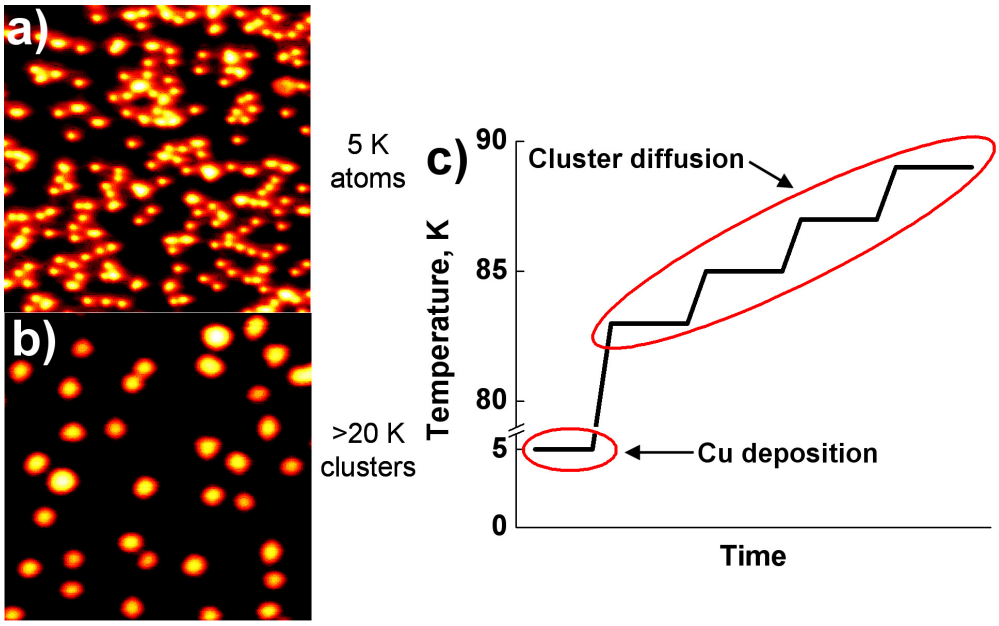

Figure 2.3 Experimental procedure. Cu was deposited at 5 K, where individual atoms could be subsequently imaged and their density precisely determined (a). Warming the STM stage above ~20 K allowed cluster formation and diffusion (b). (c) shows a temperature-time plot for a typical experiment involving Cu deposition and imaging at 5 K, and cluster diffusion measurements at multiple elevated temperatures. The improved setup allowed nucleation and diffusion events to be directly observed at any temperature between 5-300 K.

CHAPTER 3

MISFIT-DISLOCATION-MEDIATED HETEROEPITAXIAL ISLAND DIFFUSION

3.1 Introduction

Dislocations are key in the mechanical properties of solids by enabling crystalline materials to deform plastically when subjected to stress orders of magnitude lower than their theoretical critical shear stress [1]. They have also been shown to relieve stress in strained films, greatly affecting the growth mode [2-4], and have been predicted [5,6] but never experimentally implicated in adatom island diffusion. The majority of experimental studies of island diffusion have been limited to homoepitaxial systems where motion is usually a result of diffusion at steps, particularly for large islands (10^2-10^3 atoms) [7-12]. In these cases, the barrier is insensitive to size, but diffusivity scales with size depending on the rate-limiting process [13-15]. In contrast, there have been numerous theoretical predictions [16-22] and a few experimental demonstrations [23-27] of non-trivial size dependencies of the diffusion *barrier and/or prefactor* for smaller homoepitaxial clusters (2-20 atoms). This work shows that dislocations in highly-mismatched heteroepitaxial islands reduce barriers for islands of special sizes and shapes in the same way that they reduce the yield stress of bulk materials: by enabling slip to occur in a piecewise fashion.

Using scanning tunneling microscopy (STM) and molecular dynamics (MD) simulations, we reveal a dislocation-mediated island diffusion mechanism for Cu on Ag(111). Simulations show that the lattice mismatch of ~12% favors dislocation nucleation in islands larger than tetramers, resulting in a non-trivial size dependence that

is manifest in experiments where clusters containing up to 26 diffuse much faster than smaller clusters. The barriers for island sizes and shapes favoring this mechanism are lower than that for edge diffusion or Ostwald ripening, and cluster coalescence is the kinetically preferred coarsening pathway.

3.2 Experimental

Measurements were carried out in an Omicron LT-STM that can image at 5-300 K. The Ag(111) substrate was prepared in an adjoining chamber by evaporating Ag onto Si(111)-7x7 at ~20 K and annealing at ~500 K for 1-2 hours, producing large, defect-free terraces [28]. To test surface quality, diffusion barriers for atoms and dimers on these substrates were measured and are in good agreement with the published values of 65 and 73 meV, respectively [29]. The sample, held at 5 K on the STM stage, was exposed to Cu atoms. The Cu areal density, θ, was determined by counting atoms from images collected at 5 K. The STM stage was warmed to allow atom and dimer diffusion and cluster growth. From high-resolution images of a large (600) ensemble of clusters, sizes were estimated by measuring their area at X% of the cluster height. The precisely known Cu adatom density, θ, was used to adjust the parameter X until $A_{image}\theta = A_{island}\rho_{Cu(111)}$, where A_{image} is the area of the image, A_{island} is the total area of the island ensemble, and $\rho_{Cu(111)}$ is the areal density of a bulk Cu(111) plane. It is estimated that the uncertainty in island size is ±1 atom.

3.3 Experimental Results

The region of interest was imaged every 4.26 min for ~80 hours at each temperature, 80, 83, 85, and 87 K. This enabled diffusion barriers and prefactors to be measured directly for individual clusters. Fig. 3.1 shows a sequence of STM images collected at 80 K. What is interesting is that the 13-atom cluster underwent significant diffusion, while the 7- and 15-atom clusters were immobile, suggesting a "magic" size with a low diffusion barrier. There was no change in size or shape, ruling out edge diffusion or atom exchange between islands—the apparent change in shape in Fig. 3.1 is a result of an increase in scan speed after the first image. The dotted line guides the eye along the diffusion path of the 13-atom cluster. That motion occurs along the close-packed $[0\bar{1}1]$ direction is significant because fcc metals slip on {111} planes in [110] directions, suggesting a relation between the diffusion mechanism and dislocation glide.

Using a particle tracking program [30], we determine trajectories with atomic precision, as shown in Fig. 3.2 for a 10-atom cluster at 85 K. The positions occupied by the cluster centroid are plotted vertically on the left, revealing a discrete set of adsorption sites separated by the Ag nearest-neighbor distance. This shows that the cluster hops collectively between equivalent sites. If diffusion occurred through individual atomic events, hop lengths for the centroid would be a fraction of this distance and inversely proportional to island size. Diffusion measurements for the cluster in Fig. 3.2 at 83, 85, and 87 K showed that it visited 9, 12, and 20 sites after 50, 120, and 230 hops, respectively. This demonstrates that the diffusion is close to an unrestricted 1-D random walk since the number of sites visited in a walk of n hops is expected to be $(8n/\pi)^{1/2}$, which yields 11, 17, and 24 sites for the cases above [31].

The plot of position vs. time in Fig. 3.2 shows that the mean time between hops is long compared to the frame rate, ensuring that all hops are counted and mean hop rates can be measured directly. The mean hop rate for this cluster at 83, 85, and 87 K is plotted against 1/kT in the inset, giving an activation energy of 260 ± 20 meV and a prefactor of $7x10^{11\pm1.3}$ s^{-1}. The reported barrier, prefactor and related uncertainties were determined using a weighted least-squares fit, where the weighting factors and uncertainties were derived from the standard deviation of the measured time between hops and the number of hops observed [32]. Several 10-atom clusters were followed at multiple temperatures and all had barriers and prefactors within a standard error of 260 meV and 10^{12} s^{-1}.

The experiments show that low diffusion barriers are not limited to clusters larger than heptamers. Fig. 3.3 is a series of STM images showing the diffusion of a pentamer at 80 K. In this case, motion was too fast for direct hop rate measurement, but the number of distinct sites visited was determined to be 55. By assuming an unrestricted random walk with a prefactor of 10^{12} s^{-1}, the barrier was estimated to be ~210 meV. Similar measurements for 13-, 14- and 26-atom clusters at 83 K give barriers of 225, 240 and 250 meV, respectively, showing that this mechanism is viable beyond the decamer. In comparison, these diffusion barriers are much lower than the barriers for homoepitaxial island migration through edge diffusion on either Cu(111) or Ag(111), ~500 meV [12] and in the size range studied, coarsening through cluster-cluster coalescence is kinetically favored over Ostwald ripening [33-38]. The non-monotonic size dependence of the diffusion barrier is clearly more complex than the simple single magic size effect predicted by Hamilton [6] for a mismatched system.

Our diffusion model is further supported by the atomic resolution image in Fig. 3.4 collected at 100 K after a 90-second anneal to ~200 K which allowed for significant coarsening. Islands with significant mobility would have been consumed through coalescence, resulting in a size distribution dominated by low-mobility islands. Heptamers, in epitaxial orientation with the substrate, were present after the anneal and were immobile at 100 K while all other islands, many bi-layer, contained 20 or more atoms. The presence of the heptamers after the anneal indicates their low mobility relative to other clusters with sizes up to ~20 atoms, consistent with simulations that predict the heptamer to have the highest diffusion barrier among clusters containing up to 14 atoms.

3.4 Simulation Results

MD simulations were conducted to investigate the atomic processes at work. An embedded-atom method potential parameterized for Cu/Ag(111) [39] determines the diffusion barriers and mechanisms for selected islands. This potential slightly overestimates the monomer and dimer diffusion barriers, giving 93 and 88 meV, respectively. The potential is optimized to produce accurate island geometries, energies, and kinetics. High-temperature annealing allows the equilibrium island shapes to be determined. Molecular dynamics simulations and dimer method [40] search the phase-space for possible diffusion transitions, and the nudged-elastic band method [41] determines the energy barriers and the atomic-scale mechanisms.

Fig. 3.5 summarizes the MD results for 3-, 7-, 5-, and 10-atom clusters, which show that islands of certain sizes and shapes allow metastable dislocations, leading to

reduced diffusion barriers. The trimer in Fig. 3.5 (a) moves through simultaneous glide with a barrier of 287 meV, roughly three times the simulated monomer diffusion barrier. The heptamer (b) also moves in a collective fashion, though the atoms do not cross bridge sites simultaneously. In the transition state, the top right portion of the island moves towards hcp stacking prior to the lower left, reducing the barrier to 490 meV, about five times the monomer barrier.

Fig. 3.5 (c) and (d) show that a different, low-barrier mechanism involving a metastable dislocation (dotted lines) is accessible to the pentamer and decamer. The diffusion barrier for the decamer, 283 meV, is little more than half that of the heptamer and even slightly lower than the trimer barrier. The pentamer and decamer diffusion barriers, 214 and 283 meV, respectively, are in excellent agreement with the experimental values of ~210 and 260±20 meV. The overestimation of barriers in the simulations is expected, based on the monomer and dimer simulation barriers. The diffusion process for the decamer in Fig. 3.5 (d) proceeds as follows. Starting from F10, all Cu atoms in fcc sites, a metastable state with 5 atoms in hcp sites, F5H5, is accessed. The dashed line indicates a dislocation with Burgers vector $\vec{b} = 1/6[\bar{2}11]$ separating the fcc and hcp regions. If the remaining fcc atoms follow to H10, the center of mass is displaced by one Burgers vector. Symmetry allows F10 to accommodate dislocations with $\vec{b} = 1/6[\bar{2}11]$ or $\vec{b} = 1/6[1\bar{2}1]$ while H10 can accommodate $\vec{b} = 1/6[\bar{1}2\bar{1}]$ or $\vec{b} = 1/6[2\bar{1}\bar{1}]$. Thus, successive dislocation events allow for forward, backward, or zero net displacement along $[\bar{1}10]$ with equal probability and a barrier of 283 meV for a complete fcc-fcc step. This type of motion is similar to what has been called “reptation” [42,43]. The short lifetimes of H10 (~10^{-4} s) and H5F5 (~10^{-8} s) compared to F10 (on the order of

seconds) would prevent them from being observed with STM and any image of the cluster would show it in the F10 configuration. The pentamer (c) moves in an analogous manner. Despite the 3-fold symmetry of fcc {111}, the experimental trajectories presented in this paper show one-dimensional motion; however, many islands throughout the size range diffused in two dimensions with varying degrees of anisotropy from completely isotropic to highly anisotropic. This is possibly due to differing local environments resulting from surface-mediated cluster interactions.

More extensive simulations show that the low-barrier mechanism, as shown for the decamer and pentamer in Fig. 3.5, is inaccessible to closed-shell structures like the trimer and heptamer. To preserve Cu-Cu bonds, the dislocations in this process must nucleate between close-packed rows of the same length and with Burger's vectors that bring the atoms closer together [44]. This is illustrated in Fig. 3.6, which shows the differences between the low-barrier "reptation" dislocation mechanism (a) and the high-barrier "glide" dislocation mechanism (b). The "glide" mechanism is the preferred one for closed-shell structures that would require bond-breaking for "reptation" (c). This feature is also why the only dislocations allowed in the F10 or H10 configurations are $1/6[\bar{2}11], 1/6[1\bar{2}1]$ or their directional opposites. This rule means that besides island size, shape is important. There is anecdotal evidence in the experimental measurements that shape can be as important as size: some initially-immobile clusters are spontaneously mobilized subsequent to a shape change while maintaining their size.

The combined effects of size and shape are illustrated in Figure 3.7, which organizes islands into families containing the same number of sheared <110> rows; one row in blue, two rows in green, three rows in black, and four rows in red. When plotted

against the island misfit strain, the energy barriers for diffusion within each family display a "magic size" for diffusion analogous to that for Hamilton's one-dimensional model. The islands with the highest barriers within each family, indicated by the solid squares, are those with shapes that prevent the low-barrier reptation dislocation mechanism for the reasons explained above. Islands that allow reptation are indicated with the open squares. The significant effect of island shape can be illustrated by comparing the different barriers for the compact heptamer (black) to the extended heptamer (green); the barrier for diffusion of the extended structure is only ~20% that of the compact structure of the same size.

3.5 Conclusion

We have shown that a dislocation mechanism provides a pathway to coarsening through cluster diffusion for clusters as large as 26 atoms with barriers significantly lower than those for edge diffusion or Ostwald ripening. This mechanism leads to significantly reduced diffusion barriers for islands with sizes and shapes that favor metastable dislocations with the result that large islands can move more easily than smaller ones. Thus, in much the same way that dislocations reduce the yield stress of bulk metals from their theoretical values, they also reduce island diffusion barriers. It is clear that this mechanism is promoted by lattice mismatch, which reduces the energy cost of bringing the Cu atoms closer together, and it is likely a general phenomenon applicable to similarly mismatched systems.

3.6 References

1. D.Hull and D.J. Bacon, *Introduction to Dislocations* (Butterworth-Heinemann, 2001) 4th edition.
2. M. Krishnamurthy, J. S. Drucker, J. A. Venables, J. Appl. Phys. **69,** 6461 (1991).
3. D. J. Eaglesham, M. Cerullo, Phys. Rev. Lett. **64**, 1943 (1990).
4. J. Drucker, Phys. Rev. B **48**, 18203 (1993).
5. J. C. Hamilton, M. S. Daw, and S. M. Foiles, Phys. Rev. Lett. **74**, 2760 (1995).
6. J. C. Hamilton, Phys. Rev. Lett. **77**, 885 (1996).
7. K. Morgenstern, Phys. Status Solidi B **242** 773 (2005).
8. M. Giesen, Prog. Surf. Sci. **68** 1 (2001).
9. K. Morgenstern, E. Laegsgaard, and F. Besenbacher, Phys. Rev. Lett. **86** 5739 (2001).
10. K. Morgenstern, G. Rosenfeld, B. Poelsema, and G. Comsa, Phys. Rev. Lett. **74** 2058 (1995).
11. J.-M. Wen, S. L. Chang, J. W. Burnett, J. W. Evans, P. A. Thiel, Phys. Rev. Lett. **73** 2591 (1994).
12. D. C. Schlößer et al., Surf. Sci. **465** 19 (2000).
13. K. Morgenstern, E. Lægsgaard, F. Besenbacher, Phys. Rev. B **66** 115408 (2002).
14. S. V. Khare, N. C. Bartelt, T. L. Einstein, Phys. Rev. Lett. **75** 2148 (1995).
15. S. V. Khare, T. L. Einstein, Phys. Rev. B **54** 11752 (1996).
16. A. Karim, A. N. Al-Rawi, A. Kara, and T. S. Rahman, Phys. Rev. B **73** 165411 (2006).
17. J. Heinonen, I. Koponen, J. Merikoski, and T. Ala-Nissila, Phys. Rev. Lett. **82** 2733 (1999).

18. V. Papathanakos, G. A. Evangelakis, Surf. Sci. **499** 229 (2002).

19. O. S. Trushin, P. Salo, and T. Ala-Nissila, Phys. Rev. B. **62** 1611 (2000).

20. O. S. Trushin, P. Salo, and T. Ala-Nissila, Surf. Sci. **482-485** 365 (2001).

21. C. M. Chang, C. M. Wei, and S. P. Chen, Phys. Rev. Lett. **85** 1044 (2000).

22. U. Kürpick, B. Fricke, G. Ehrlich, Surf. Sci. **470** L45 (2000).

23. G. L. Kellogg, Phys Rev. Lett. **73** 1833 (1994).

24. S. C. Wang, G. Ehrlich, Surf. Sci. **239** 301 (1990).

25. G. L. Kellogg, Appl. Surf. Sci. **67** 134 (1992).

26. H.-W. Fink, G. Ehrlich, Surf. Sci. **150** 419 (1985).

27. S. C. Wang, U. Kürpick, G. Ehrlich, Phys. Rev. Lett. **81** 4923 (1998).

28. L. Huang, S. J. Chey, J. H. Weaver, Surf. Sci. **416** L1101 (1998).

29. K. Morgenstern, K.-F. Braun, K.-H. Rieder, Phys. Rev. Lett. **93** 056102 (2004).

30. J. C. Crocker and D. G. Grier, J. Colloid Interface Sci. **179**, 298 (1996).

31. J. Rudnick, and G. Gaspari, *Elements of the Random Walk* (Cambridge University Press, 2004), pp. 63-67.

32. R. J. Cvetanovic and D. L. Singleton, J. Phys. Chem. **83** 50 (1979).

33. J. –M. Wen, J. W. Evans, M. C. Bartelt, J. W. Burnett, P. A. Thiel, Phys. Rev. Lett. **76** 652 (1996).

34. K. Morgenstern, G. Rosenfeld, G. Comsa, Phys. Rev. Lett. **76** 2113 (1996).

35. K. Morgenstern, et al., Phys. Rev. Lett. **80** 556 (1998).

36. G. S. Icking-Konert, M. Giesen, H. Ibach, Surf. Sci. **398** 37 (1998).

37. J. B. Hannon, et al., Phys. Rev. Lett. **79** 2506 (1997).

38. G. Rosenfeld, et al., Surf. Sci. **402** 401 (1998).

39. H. H. Wu and D. R. Trinkle, Comp. Mater. Sci. **47,** 577 (2009).

40. G. Henkelman and H. Jónsson, J. Chem. Phys. **111**, 7010 (1999).

41. G. Mills and H. Jónsson, Phys. Rev. Lett. **72**, 1124 (1994).

42. V. Chirita, E. Munger, J. Greene, and J.-E. Sundgren, Surf. Sci. Lett. **436**, L641 (1999).

43. V. Chirita, E. Munger, J. Greene, and J.-E. Sundgren, Thin Solid Films **370**, 179 (2000).

44. H. H. Wu, A. W. Signor, and D. R. Trinkle, J. Appl. Phys. **108** 023521 (2010).

3.7 Figures

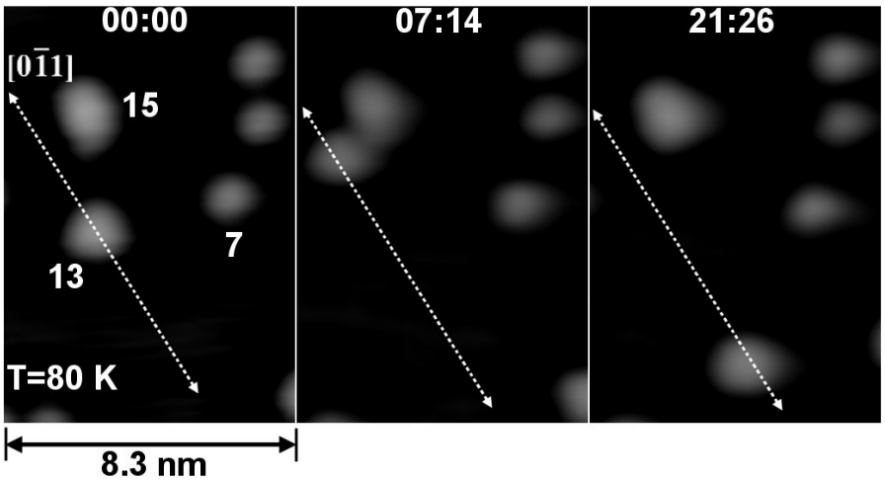

Figure 3.1 Anomalous diffusion of Cu cluster on Ag(111) at 130 K. The 15-20 atom cluster indicated underwent significant diffusion while smaller and larger clusters were completely immobile. Cluster diffusion occurred in the absence of shape changes or atom exchange between clusters, in contrast to homoepitaxial island diffusion on Ag(111) or Cu(111).

.

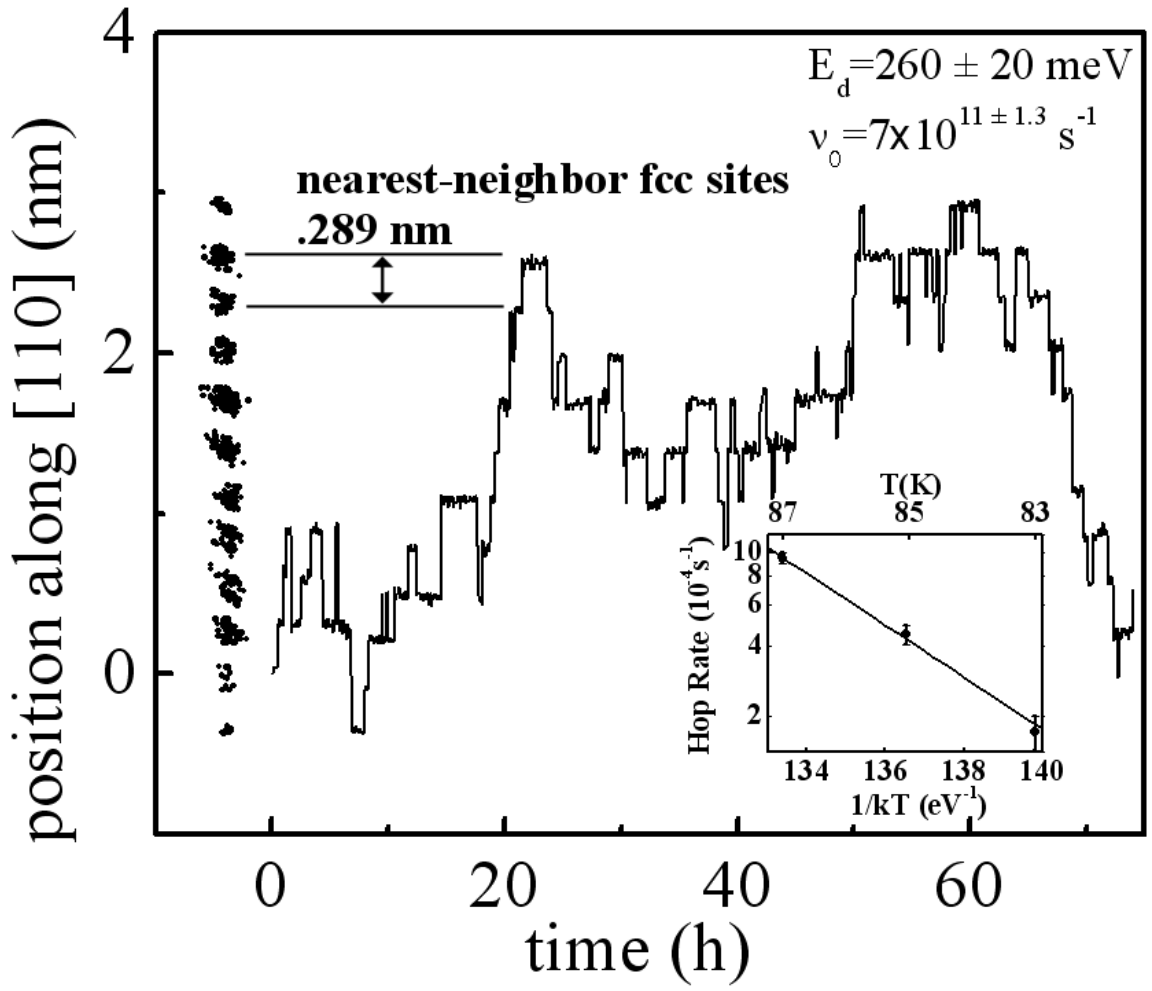

Figure 3.2 Diffusion trajectory for a 10 atom cluster doing a 1-D walk along [110] at 85 K. Each point on the left represents the cluster's centroid from a data set containing ~1100 frames. The plot as a function of time makes it possible to determine the mean hop rate. In the inset, the temperature dependence of the hop rate yields an activation energy of 260 ± 20 meV, and an attempt frequency of $7x10^{11\pm1.3}$ s^{-1}.

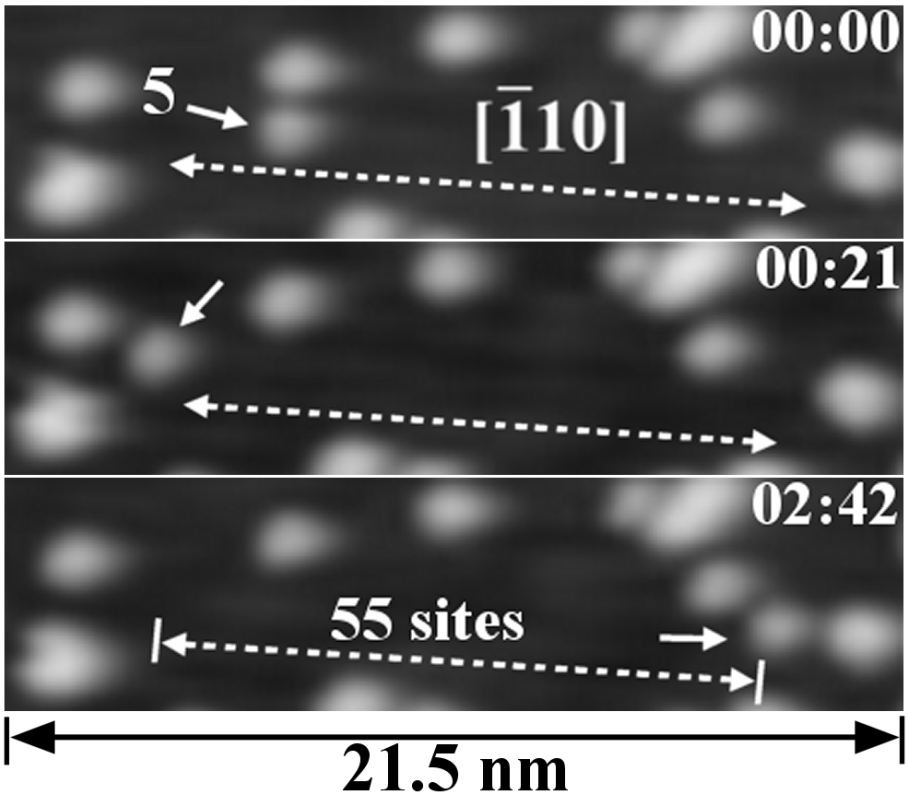

Figure 3.3 STM images (-200 mV, 0.5 nA) showing diffusion of a 5-atom cluster at 80 K. The relative times of the images are given in h:min. While pentamer diffusion at 80 K was too fast for direct hop rate determination, the barrier was estimated to be ~210 meV, assuming an unrestricted random walk.

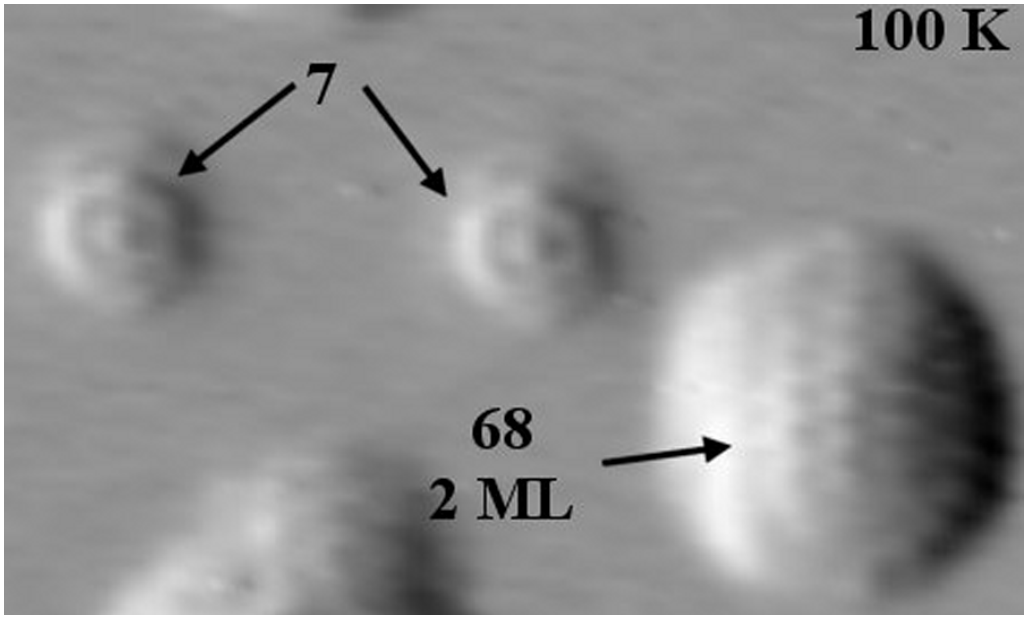

Figure 3.4 Atomic resolution image at 100 K after a ~90 sec anneal at ~200 K. Heptamers survived the anneal and were immobile at 100 K. The other clusters on the surface contained 20 or more atoms, having formed from cluster-cluster coalescence. Many bi-layer islands were present, like the 68-atom island shown.

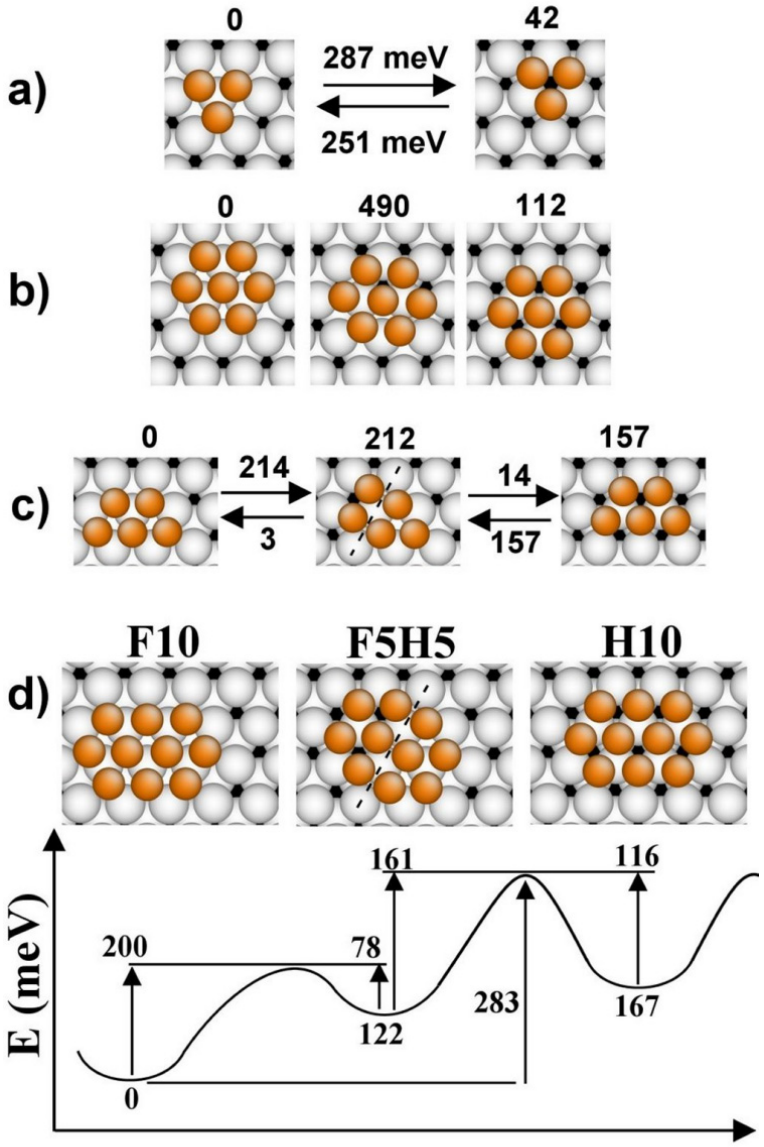

Figure 3.5 Molecular dynamics simulations of 3-, 7-, 5-, and 10-atom Cu clusters on Ag(111). The trimer (a) migrates via simultaneous glide, with all atoms moving across bridge sites at the same time. The heptamer (b) moves in a dislocation-like mechanism, where the transition state contains atoms in both fcc and hcp sites. The pentamer (c) and decamer (d) diffuse via a different misfit dislocation mechanism, where the states containing the dislocation are metastable and the dislocation lines are oriented along [110]. All energy values are given in meV.

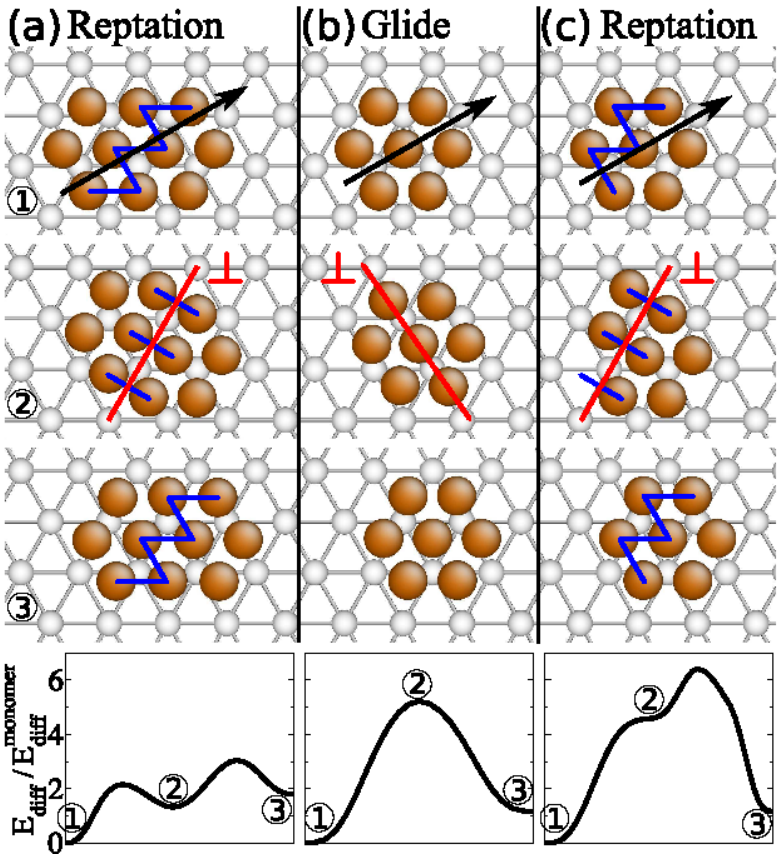

Figure 3.6 Geometric requirements for the low-barrier "reptation" mechanism. △indicates the fcc sites and ▽ indicates hcp sites. An allowed "reptation" dislocation transition is shown in (a) as the left half of the island shifts into hcp stacking without breaking Cu-Cu bonds. (b) illustrates the high-barrier "glide" dislocation diffusion mechanism for closed-shell structures. The high-barrier "glide" mechanism is preferred for these structures because a "reptation" dislocation would require the breaking of Cu-Cu bonds, increasing the barrier as shown in (c). The energy barriers, normalized with respect to the EAM monomer diffusion barrier, are illustrated at the bottom. Note, the "reptation" dislocation is metastable, while the "glide" dislocation is not.

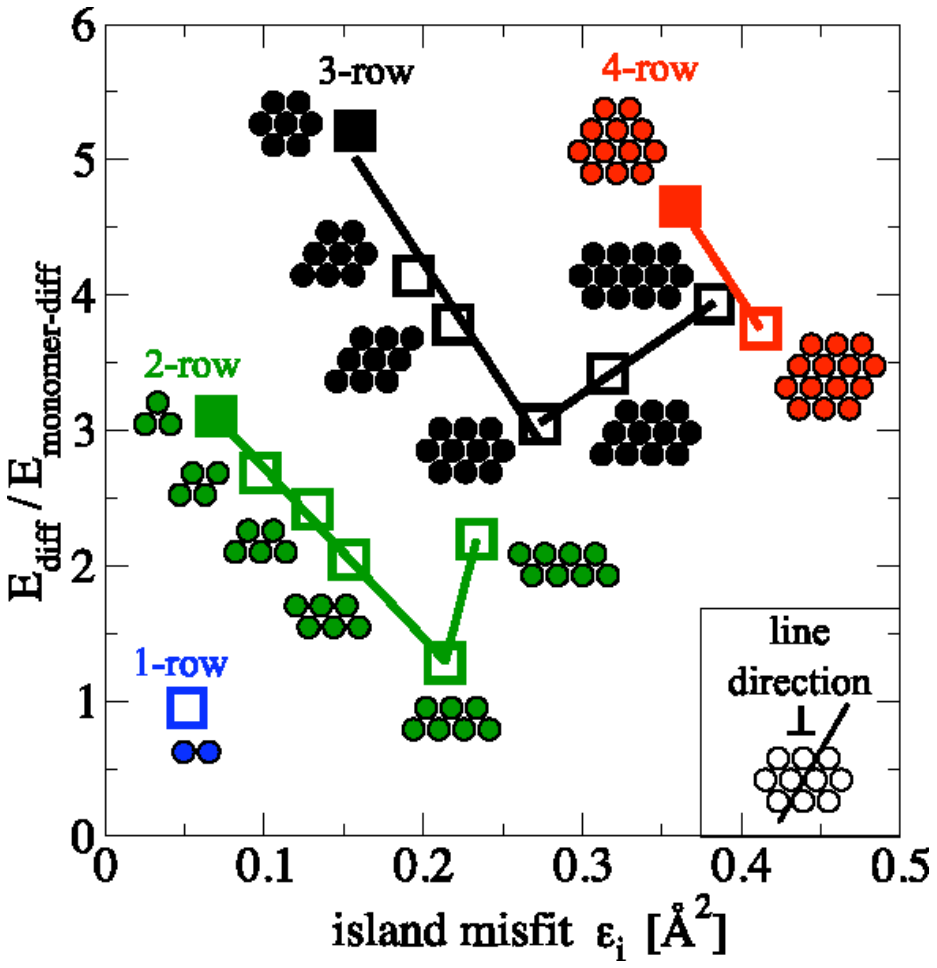

Figure 3.7 Island diffusion barriers plotted against island misfit strain showing a shape-modulated magic-size effect. Diffusion barriers are normalized with respect to the EAM monomer diffusion barrier of 93 meV. The open squares represent islands with shapes that allow reptation, while the filled squares represent islands with shapes that do not. Islands, when organized into families with the same number of sheared <110> rows (1, blue; 2, green; 3, black; 4, red) follow a "magic size" trend in the diffusion barrier. Grouping the islands into families according to the number of rows highlights the key role of shape. Note the significantly different barriers for, e.g. the compact heptamer (black) vs. the extended heptamer (green). The 7- and 8- atom 2-row configurations are not the ground-state ones, but are shown to illustrate the continuation of the magic size trend.

CHAPTER 4

PREFERENTIAL NUCLEATION AND HIGH MOBILITY OF LINEAR Cu TRIMERS ON Ag(111)

4.1 Introduction

Surface diffusion of atoms and clusters has been studied for decades, driven in large part by the importance of the processes leading to mass transport on surfaces. This work has revealed a diversity of surface diffusion phenomena, especially for cluster diffusion because of the numerous ways a collection of atoms can move on a surface [1-4]. The mobility of small clusters can have significant implications on the nucleation density and island size distribution in the early stages of growth [5-9], and the diffusion of large islands leads to coarsening in the late stages [10-18].

Despite their importance, relatively little direct, quantitative experimental work has been done regarding the stability and diffusion of small clusters. Because the majority of cluster diffusion studies have focused on homoepitaxial systems, even less is known about the role of lattice mismatch in determining the properties of heteroepitaxial clusters despite predictions of interesting phenomena [19, 20]. While the mobility of larger islands generally decreases with size, several cases of non-monotonic size dependencies [21-32] and, remarkably, cases where clusters have even higher mobility than individual atoms, have been reported [27-32].

In this paper, we focus on Cu trimers on Ag(111) and demonstrate that, depending on their structure, they can have significantly more mobility than either atoms or dimers. Using low-temperature scanning tunneling microscopy (STM), we have previously

shown that larger clusters have surprisingly low diffusion barriers and a novel dislocation mechanism that is related to the ~12% lattice mismatch for Cu on Ag(111) [25, 26]. Here, we show that Cu trimers diffuse large distances following their formation. Studies at 24 K show that this trimer mobility is transient, and the mobile trimers are equilibrated in a compact, immobile state or coalesce with other particles. To determine the structure of the mobile precursor, we used the STM tip to construct both compact and linear chain trimers at 5 K. The linear chain trimers underwent lengthwise hopping along the close-packed <110> directions and rotated about an end atom at $T \geq 8$ K while maintaining a linear shape. The hop and rotation rates were measured between 8-12 K, yielding a diffusion barrier of 13.6 meV, only ~1/5 the diffusion barrier of individual atoms, 65 meV. In contrast, the compact trimer constructed at 5 K was immobile. We conclude that the large displacements upon trimer formation are due to a precursor, namely the linear trimer. The linear trimer has a very low diffusion barrier, making it an important contributor to mass transport for Cu on Ag(111). The broader and more surprising implication of this work is that significant diffusion of a non-equilibrium cluster can occur before the equilibrium structure is reached. Furthermore, while previous reports of transient mobility have been related to the enthalpy released upon condensation, our results point to a case of transient mobility results from a non-equilibrium structure that is favored upon cluster nucleation.

4.2 Experimental

Experimental measurements were carried out in an Omicron low-temperature scanning tunneling microscope that operates at 5-300 K. The Ag(111) substrates were

thick films (100's of monolayers) grown in a preparation chamber (base pressure ~4×10^{-11} Torr) by evaporating Ag onto Si(111)-7×7 at ~20 K, followed by an anneal at ~600 K for a few seconds. These films have large, flat regions free of defects or steps [33], making them ideal for diffusion studies. The excellent agreement between our measurements of Cu atom and dimer diffusion barriers with those measured on Ag(111) single crystals [34] indicate a high quality surface. This also provides a confirmation of temperature accuracy.

Once the substrate was prepared, the sample was moved to the STM stage and cooled to ~5 K. A homebuilt evaporator attached to the measurement chamber enabled deposition of dilute amounts of Cu while the sample was on the STM stage at 5 K. The Cu source was heated in a W basket, and the exterior of the evaporator was water-cooled to minimize outgasing. During evaporation, the pressure remained below 10^{-10} Torr. A small aperture created a narrow beam, protecting the critical components of the microscope and limiting exposure to the sample surface. A quartz crystal microbalance mounted in the evaporator was used to monitor the flux, and it was calibrated by counting individual atoms in STM images collected at 5 K immediately after exposure. This, combined with a shutter, allowed for precise control of the amount of Cu, and it enabled the early stages of nucleation and growth to be observed *in situ* as the sample was warmed from 5 K.

To construct compact and linear trimers at 5 K, the tip was positioned above the atom to be moved and the tunneling parameters were changed to bring it close enough to allow an attractive interaction. The tip was then moved at ~1 nm s^{-1} to the desired location, pulling the atom along with it. To release the atom, the tunneling parameters

were reset to those used for imaging (0.5 V, 0.3 nA). To establish the optimal tunneling conditions, manipulation attempts were repeated while the tunneling current was gradually increased, bringing the tip incrementally closer to the surface, until a successful manipulation was achieved. The optimal parameters for manipulation were 0.5 V and 6.0 ±1 nA, though the parameters and success rate varied depending on the condition of the tip. This procedure was adapted from those used in other studies of fcc(111) metals surfaces [35, 36].

4.3 Trimer Nucleation and Rapid Diffusion

Figure 4.1 presents a series of images collected at 24 K that show trimer nucleation and subsequent rapid displacement. The labels indicate the number of atoms in each particle, a number that is known precisely because cluster formation events were observed directly, starting from individual atoms. For the atoms and dimers, diffusion barriers match previously published values [34]. The images in Fig. 4.1 were selected from a set of ~150 with ~215 s between frames (~9 hours of imaging). In (a), the ellipses highlight atom-dimer pairs in close proximity, prior to their combination. During the time between frames, the resulting trimers moved 2 nm or 15 nm to the positions indicated and coalesced with a dimer or atom to form the pentamer and tetramer shown in (b). Note that image (b) of "32 min" was selected to show the small and slower displacements of the atoms and dimers in the viewing area. The highlighted atom-dimer pair in (b) had combined in the next image (c) and had moved 6 nm before being immobilized without coalescence. This trimer and all others that were immobilized had

compact shapes, and they were stable during the measurement time of several days at 20-24 K.

Figure 4.1(d) summarizes the displacements for 39 trimer formation events. The points represent the coordinates of the final location referenced to those of the atom-dimer pairs immediately prior to coalescence. The (red) triangles represent four trimers that were immobilized on the pristine surface, as in (c), and the black circles represent those that ultimately coalesced with other ad-particles, as in (b). The displacements ranged from 2-20 nm and all occurred within the time between images (80-215 s). Since the atom and dimer positions were continuously monitored, we can conclude that all trimer formation events resulted in rapid diffusion.

From Fig. 4.1, it is clear that trimer nucleation results in a cluster that has significantly more mobility than atoms or dimers. The fact that several trimers were immobilized on the surface without encountering other ad-species demonstrates that their intrinsic mobility is short-lived. While it is possible that they were trapped at undetectable defects on the surface, one would expect atoms and dimers to be trapped as well, yet they all maintained the expected diffusivity. Furthermore, in one instance, a diffusing atom probed the future resting site of a trimer without any change in its diffusion properties, strengthening the case that the trimers are immobilized on a pristine surface, that the mobility is naturally transient, and that there is something special about the trimer formation event that leads to a very mobile species that ultimately converts to the immobile trimer.

Based on the data of Fig. 4.1(d), the mean-squared displacement is 44.6 nm. Assuming two-dimensional diffusion, we can deduce a lower limit on the diffusivity of

the mobile precursor using the Einstein relation, $D = \left\langle \Delta r^2 \right\rangle / 4\tau$, where $\left\langle \Delta r^2 \right\rangle$ is the mean squared displacement and τ is the time between images. It is important to note that this estimation provides only a lower limit on the diffusivity since, with the experimental time resolution, we only observe initial and final locations. Based on this analysis, the lower limit on the diffusivity is ~5×10^{-16} $cm^2 s^{-1}$, compared to ~4×10^{-18} $cm^2 s^{-1}$ for atoms. Assuming the normal prefactor of 10^{-3} $cm^2 s^{-1}$, this establishes an upper limit on the diffusion barrier of ~58 meV compared to 65 meV for individual atoms, though it is possibly much lower than that. This low barrier is surprising in light of molecular dynamics simulations that predict a barrier of ~290 meV—prohibitively large to allow diffusion at 24 K [25, 26, 37]. In these simulations, the ground state of a Cu trimer on Ag(111) was a compact triangle with all atoms in fcc sites, and diffusion occurred in a concerted fashion. In agreement with the simulations, compact trimers were immobile at 24 K.

While the above has considered thermal diffusion, there is the possibility that a contribution to displacement might arise from the energy associated with bond formation upon dimer and atom binding. This is unlikely since nucleation of dimers and larger particles never resulted in movement. From Fig. 4.1 (d), the mean trimer displacement is 5.9, with some displacements as large as ~20 nm. An estimate of the bond formation energy based on the bulk Cu cohesive energy (3.49 eV/atom) is 0.29 eV for forming a single bond (atom attaching to end of dimer) and 0.58 eV for two bonds (forming a triangular trimer). In contrast, the dissociative chemisorption of O_2 on Al(111) results in a ~7 eV energy gain (3.5 eV/atom), but the average O atom displacement was only 4 nm [38-40]. Furthermore, later experiments ruled out any significant transient mobility of O

atoms during the dissociative chemisorption of O_2 on Al(111) [41]. We conclude that the contribution from the formation enthalpy is small and cannot account for the large displacements observed for Cu_3, a much heavier particle than Oxygen.

4.4 Mobile Linear and Immobile Compact Trimers

From the data of Fig. 4.1, one cannot conclude much regarding the nature of the precursor; only the initial and final locations are known. Given the predicted and experimentally-observed stability of compact trimers, we reasoned that the mobile precursor has a different structure. To learn more about the structure of the mobile trimer presented considerable experimental challenges. At temperatures where trimers form on the experimental time scale, their mobility is too high and too short-lived to allow structural investigations. Accordingly, we reduced the temperature and used the STM tip to manipulate individual atoms, as outlined above, to construct linear and compact trimers. Figure 4.2 shows the construction of a linear trimer at 5 K. Three Cu monomers are indicated in (a). The atom on the left was brought into contact with the middle atom in (b). The orientation of the dimer was established, and the third atom was moved to the end of the dimer in (c), forming a linear trimer oriented along the close-packed $[0\bar{1}1]$ direction. The linear trimer was stable and immobile at 5 K.

To investigate the properties of linear trimers, we increased the temperature while continuously imaging. Significantly, the temperature at which trimer motion was first observed was 8 K, extremely low compared to the 19 K onset for adatom motion. Two types of motion occurred with equal probability in the 8-9 K range, namely lengthwise hopping along close-packed <110> directions and rotation about an end-atom. Although

rotations about each end had equal probability, rotation about the middle atom was never observed. The images in Fig. 4.3 obtained at 8.5 K show the changes in orientation associated with rotation. The chain is oriented along $[\bar{1}10]$ in (a), $[0\bar{1}1]$ in (b), and $[\bar{1}01]$ in (c). The ellipses help distinguish the different orientations. A particle tracking program [42] was used to extract the trimer trajectory and nearby immobile atoms were used as a reference to correct for drift of the microscope. Figure 4.3 (d) is a representative trajectory of one of the linear trimers, comprised of a discrete set of adsorption sites separated by the Ag(111) nearest-neighbor distance, 0.289 nm. Because rotation only occurred about an end-atom, both rotation and lengthwise hopping displace the center of mass by one nearest-neighbor spacing.

The low time resolution of the STM prevents direct knowledge of the intermediate steps in trimer chain diffusion, but important details of the intermediate steps can be inferred from the experimentally-observed characteristics of lengthwise translation and end-atom rotation. The fact that rotation and lengthwise hopping occur at the same rate suggests that they share the same rate-limiting step. Moreover, the rotation direction depends on both the chain orientation and on which end of the chain moves. This dependence is illustrated in the models below the images in Fig. 4.3. Below (a), for example, two rotations are allowed. The other two rotations in the upward directions were not allowed. The key to such motion must be in the intermediate steps, because the disallowed rotations would result in final states that are equivalent to those resulting from the allowed rotations. The solid circles indicate the initial atom locations, the open circles the final locations, and the arrows indicate the directions of rotation.

For larger islands of Cu on Ag(111), diffusion occurred through the nucleation of misfit dislocations that shifted a portion of the atoms into hcp sites and shortened Cu-Cu bonds, reducing strain. Applying this rule to trimer chains results in exactly the rotation directions observed experimentally, as rationalized in Fig. 4.4 which illustrates possible pathways for lengthwise hopping (a-d) and end-rotation (a,e,f) that share a step involving hcp sites that shorten Cu-Cu bonds. In this model, both hopping and rotation commence when two atoms shift into hcp sites, shown in the equivalent transitions of a-b and a-e. For lengthwise hopping, this state is followed by one in which the third atom moves into an hcp site (b), and the hop of one nearest-neighbor distance is completed by a similar piecewise motion of the trimer from hcp to fcc sites (c,d). For rotation to occur, instead of the third atom moving into hcp stacking, the two atoms in hcp sites move further as shown in (e). In this model, rotation only occurs in certain directions because rotation in the other directions would require the use of hcp sites that stretch the already strained Cu-Cu bonds, as illustrated in Fig. 4.4 (g). The sequences shown in Fig. 4 cannot be verified experimentally, but they satisfy the requirement that an intermediate step involves hcp sites to shorten Cu-Cu bonds, and this is the only explanation for the observed rotation directions. Furthermore, motion occurs in a piecewise fashion, as concerted hopping and rotation would show no preference for certain hopping and rotation directions.

An individual linear trimer was tracked between 8.34 K and 9.34 K, and Fig. 4.5 summarizes the temperature dependence of its lengthwise hop and rotation rates. The error bars represent the standard errors of the mean hop rates, and the numbers beside each point indicate the number of events observed. Both hopping (blue squares) and rotation (red triangles) occurred with nearly equal probability at each temperature

investigated and thus, when treated separately, the measured barriers and prefactors are within a standard error of each other: $\nu_o^h = 2.1\times10^{4\pm0.5}\ \mathrm{s}^{-1}$, $E_a^h = 12.7\pm1\ \mathrm{meV}$; $\nu_o^r = 3.0\times10^{5\pm0.8}\ \mathrm{s}^{-1}$, $E_a^r = 14.8\pm1.5\ \mathrm{meV}$. Because both rotation and lengthwise hopping resulted in displacement of the trimer center of mass by 0.289 nm, the overall diffusion rate (black circles) includes both hopping and rotation events with $\nu_o^d = 1.3\times10^{5\pm0.4}\ \mathrm{s}^{-1}$ and $E_a^d = 13.6\pm0.7\ \mathrm{meV}$. The barriers, prefactors, and related uncertainties were determined using a weighted least-squares fit, where the weighting factors and uncertainties were derived from the standard deviation of the measured time between hops and the number of hops observed [43]. Surprisingly, the diffusion barrier for linear trimers is only ~1/5 of that for a Cu adatom on Ag(111), 65 meV. Though the prefactors are significantly lower than the ~10^{12} s^{-1} commonly observed for diffusion, experimental measurements of atom and cluster diffusion have reported prefactors spanning a range of ~6 orders of magnitude [1, 2, 23, 44, 45].

The finite scan rate of the STM limits the temperature window where hop rates can be measured directly. To minimize the errors in barriers and prefactors, large numbers of events were observed at each temperature. To test how well the fit could predict diffusion rates at higher temperatures, we measured the mean square displacement at 12 K, a temperature where multiple hops occurred between images, and the diffusion rate fell within a standard error of the extrapolated fit. Besides verifying that the parameters measured at 8-9 K made reasonable predictions, the measurements of mean square displacements at elevated temperatures indicate that the tip had no significant influence on the measurements. Finally, to check the reproducibility of our results, we constructed a second linear trimer. It displayed the same rotation and lengthwise hopping

and the same temperature dependence of the diffusion rate, as shown by the stars in Fig. 4.4.

A compact triangular trimer was also constructed at 5 K, as shown in Fig. 4.6. Three monomers are visible in (a), a dimer is formed in (b), and a compact trimer in (c). The inset in (c) is an image of a linear trimer for a comparison. Temperature-dependent measurements to 15 K showed that the compact trimer was immobile, as expected from the measurements at 24 K. No transition to the linear form was observed. Measurements with the linear trimers likewise showed no transitions to the compact structure. We conclude that hopping and rotation at 8-9 K do not involve interconversion between linear and compact forms, in agreement with our model.

We have shown that the diffusion barrier of a linear trimer is low enough to account for the displacements observed upon trimer nucleation at 24 K. Because every trimer nucleation event resulted in rapid relocation, this implies that the kinetically preferred pathway to the compact trimer involves the linear trimer. Besides translating, Cu dimers on Ag(111) undergo rotation among the three equivalent fcc sites surrounding a surface atom, resulting in three different orientations along the close-packed <110> directions. While the barrier for dimer diffusion is higher than that for atom diffusion, the barrier for dimer rotation is lower than that for atom diffusion. Morgenstern et al. [34, 46] showed that surface-mediated adatom-dimer interactions perturb dimer rotation. With adatom-dimer separations of ~1-2 nm (4-8 lattice spacings), one dimer orientation was favored over the other two. From the data presented in [34], and especially the supporting STM movies of [46], the preferred orientation is one that presents the end of a dimer, rather than the side, toward the third atom. The relatively low barrier for dimer

rotation compared to atom diffusion would allow the dimer to rotate to the favored orientation upon the approach of a third atom. Thus, these surface-mediated atom-dimer interactions are likely the cause for the very strong bias in favor of linear trimer formation as a precursor to the thermodynamically favored compact trimer.

4.5 Conclusion

The types of motion reported here for trimers are very different from those reported in either experimental or theoretical studies of homoepitaxial fcc(111) trimers. For Ir_3 on Ir(111), both linear and triangular forms were observed, rotation required interconversion between the two forms, and translation was roughly four times more probable than rotation. Further, the mechanisms for Ir_3 do not limit center of mass displacements to one nearest neighbor distance, as we observe for Cu_3, but allow shorter displacements as well [22]. Molecular dynamics simulations of Al_3 on Al(111) show that trimer diffusion is similar to Ir_3, with interconversion between triangular and linear forms having barriers similar to those for translation [47]. Molecular dynamics simulations of Cu_3 on Cu(111) show that diffusion occurs through concerted gliding and rotation of the triangular form because this has a much smaller barrier than interconversion to the linear form [48].

In contrast, our results show that linear trimer chains on Ag(111) diffuse through lengthwise translation and end-atom rotation, which occur with equal probability, with no conversion to the compact form. Compact trimers are stable and immobile up to at least 24 K, indicating high barriers for translation and conversion to the linear form. The extremely low diffusion barrier for the linear trimer, combined with the preference for

this structure during nucleation, make the trimer an extremely important contributor to mass transport for Cu on Ag(111). The effects of lattice mismatch are manifest in the observed directions of hopping and rotation that require intermediate steps involving trimers of mixed fcc-hcp character that shorten Cu-Cu bonds to relieve strain, in a one-dimensional analog of the misfit-dislocation mechanism responsible for the low diffusion barriers of larger Cu clusters on Ag(111) [25, 26]. Because the novel diffusion phenomena for both small and large clusters of Cu on Ag(111) result from lattice mismatch, it is likely that similar behavior will occur in other heteroepitaxial systems.

4.6 References

1. G. Ehrlich, Surf. Sci. **246**, 1 (1991).
2. T. T. Tsong, Rep. Prog. Phys. **51, 759** (1988).
3. A. G. Naumovets and Z. Y. Zhang, Surf. Sci. **500**, 414 (2002).
4. A. G. Naumovets and Z. Y. Zhang, Physica A **357**, 189 (2005).
5. J. Venables, Philos. Mag. **27**, 697 (1973).
6. J. Villain, A. Pimpinelli, L. Tang, and D. Wolf, J. Phys (France) I **2**, 2107 (1992).
7. M. C. Bartelt, S. Günther, E. Kopatzki, R. J. Behm, and J. W. Evans, Phys. Rev. B **53**, 4099 (1996).
8. G. Rosenfeld, A. F. Becker, B. Poelsma, L. K. Verheij, G. Comsa, Phys. Rev. Lett. **69**, 917 (1992).
9. S. B. Lee, Phys. Rev. B **73**, 035437 (2006).
10. K. Morgenstern, Phys. Status Solidi B **242** 773 (2005).
11. M. Giesen, Prog. Surf. Sci. **68** 1 (2001).

12. K. Morgenstern, E. Laegsgaard, and F. Besenbacher, Phys. Rev. Lett. **86** 5739 (2001).

13. K. Morgenstern, G. Rosenfeld, B. Poelsema, and G. Comsa, Phys. Rev. Lett. **74** 2058 (1995).

14. J.-M. Wen, S. L. Chang, J. W. Burnett, J. W. Evans, and P. A. Thiel, Phys. Rev. Lett. **73** 2591 (1994).

15. D. C. Schlößer et al., Surf. Sci. **465** 19 (2000).

16. K. Morgenstern, E. Lægsgaard, and F. Besenbacher, Phys. Rev. B **66** 115408 (2002).

17. S. S. V. Khare, N. C. Bartelt, and T. L. Einstein, Phys. Rev. Lett. **75** 2148 (1995).

18. S. V. Khare and T. L. Einstein, Phys. Rev. B **54** 11752 (1996).

19. G. L. Kellogg, Phys Rev. Lett. **73** 1833 (1994).

20. J. C. Hamilton, M. S. Daw, and S. M. Foiles, Phys. Rev. Lett. **74**, 2760 (1995).

21. J. C. Hamilton, Phys. Rev. Lett. **77**, 885 (1996).

22. S. C. Wang and G. Ehrlich, Surf. Sci. **239** 301 (1990).

23. G. L. Kellogg, Appl. Surf. Sci. **67** 134 (1992).

24. S. C. Wang, U. Kürpick, G. Ehrlich, Phys. Rev. Lett. **81** 4923 (1998).

25. H. H. Wu, A. W. Signor, and D. R. Trinkle, J. Appl. Phys. **108** 023521 (2010).

26. A. W. Signor, H. H. Wu, and D. R. Trinkle, Surf. Sci., accepted for publication.

27. H.-W. Fink and G. Ehrlich, Surf. Sci. **150** 419 (1985).

28. W. R. Graham and G. Ehrlich, Phys Rev. Lett. **31**, 1407 (1973).

29. W.R. Graham and G. Ehrlich, J. Phys. F: Metal Phys. **4**, L212 (1974).

30. K. Stolt, W. R. Graham, and G. Ehrlich, J. Chem. Phys. **65**, 3206 (1976).

31. T. Sakata and S. Nakamura, Surf. Sci. **51**, 313 (1975).

32. B. G. Briner, M. Doering, H.-P. Rust, and A. M. Bradshaw, Science **278**, 257 (1997).

33. L. Huang, S. J. Chey, and J. H. Weaver, Surf. Sci. **416** L1101 (1998).

34. K. Morgenstern, K.-F. Braun, and K.-H. Rieder, Phys. Rev. Lett. **93**, 056102 (2004).

35. S.-W. Hla, K.-F. Braun, and K.-H. Rieder, Phys. Rev. B **67**, 201402(R) (2003).

36. J. Repp, G. Meyer, K.-H. Rieder, and P. Hyldgaard, Phys. Rev. Lett. **91**, 206102 (2003).

37. H. H. Wu and D. R. Trinkle, Comp. Mater. Sci. **47**, 577 (2009).

38. H. Brune, J. Wintterlin, R. J. Behm, and G. Ertl, Phys. Rev. Lett. **68**, 624 (1992).

39. J. Wintterlin, R. Schuster, and G. Ertl, Phys. Rev. Lett. **77**, 123 (1996).

40. A. Groß, Phys. Rev. Lett. **103**, 246101 (2009).

41. M. Schmid, G. Leonardelli, R. Tscheließnig, A. Biedermann, P. Varga, Surf. Sci. Lett. **478**, L355 (2001).

42. J. C. Crocker and D. G. Grier, J. Colloid Interface Sci. **179**, 298 (1996).

43. J. Cvetanovic and D. L. Singleton, J. Phys. Chem. **83** 50 (1979).

44. G. L. Kellogg, T. T. Tsong, and P. Cowan, Surf. Sci. **70**, 485 (1978).

45. A. J. Heinrich, C. P. Lutz, J. A. Gupta, and D. M. Eigler, Science **298**, 1381 (2002).

46. K. Morgenstern, New Journal of Physics **7**, 139 (2005).

47. C. M. Chang, C. M. Wei, and S. P. Chen, Surf. Sci. **465**, 65 (2000).

48. A. Karim, et al., Phys. Rev. B **73**, 165411 (2006).

4.7 Figures

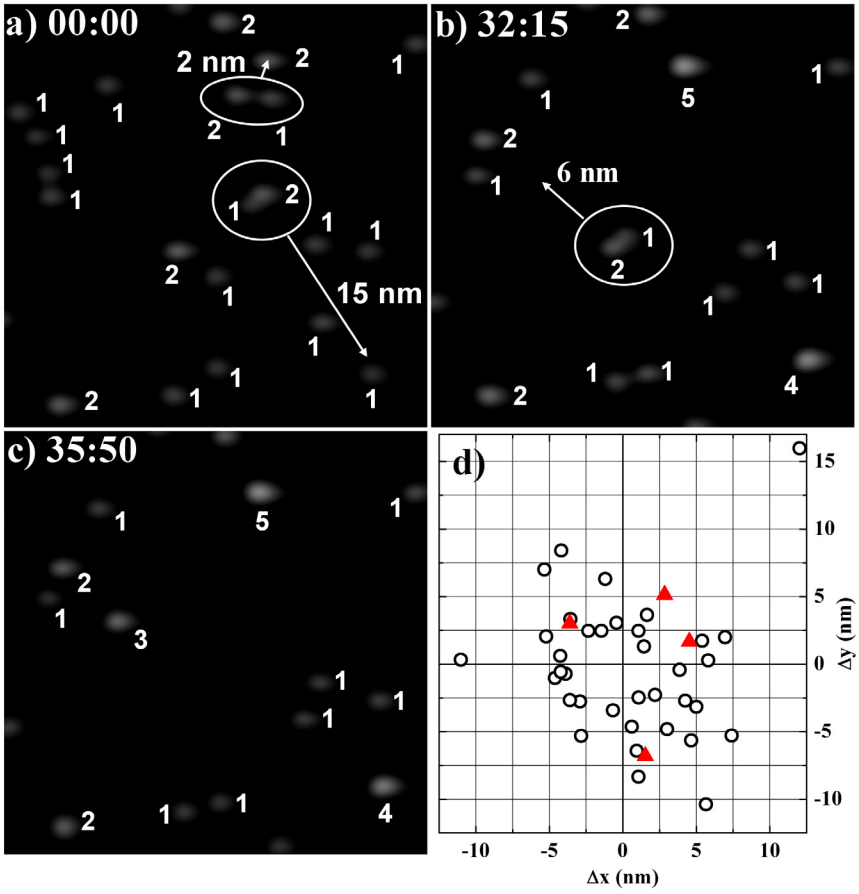

Figure 4.1 Diffusion of Cu atoms, dimers, and trimers on Ag(111) at 24 K. The labels indicate particle size, the ellipses indicate particles prior to coalescence, and arrows show the relocation of trimers upon their formation. Between (a) and (b), the highlighted pairs combined and moved to coalesce with other particles. The trimer formed between (b) and (c) was immobilized on the pristine surface. Every trimer formation event resulted in rapid displacement on a scale shorter than the time between images. The displacement vectors for all trimer formation events are plotted in (d), where the symbols represent the coordinates of the final location, referenced to the location of the atom-dimer pair prior to coalescence. The black circles represent trimers that coalesced with other particles, the red triangles represent trimers that were spontaneously immobilized. As discussed in the text, trimer formation produced mobile linear chains and conversion of those chains to compact structures immobilized them.

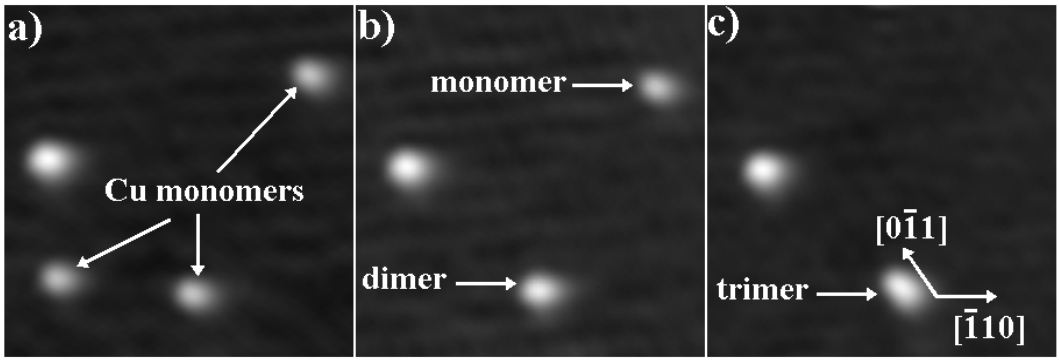

Figure 4.2 Assembly of a linear-chain trimer using the STM tip at 5 K. Starting with three Cu atoms, (a), the atom on the left was brought into contact with the middle atom, forming a dimer, (b). In (c), the third atom was moved to form a linear trimer chain oriented along $[0\bar{1}1]$. The trimer chain was stable and immobile at 5 K. Imaging parameters 0.5 V, 0.3 nA. Manipulation parameters 0.5 V, 6.0 nA.

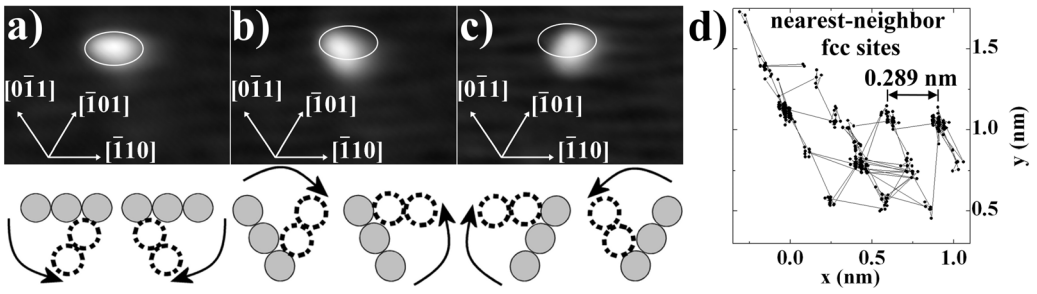

Figure 4.3 Rotation and diffusion of linear trimers at 8.5 K. The trimer orientation is [$\bar{1}$10] in (a), [0$\bar{1}$1] in (b), and [$\bar{1}$01] in (c). Hopping along the long axis and rotation about an end atom occur with equal probability. Rotation reorients the trimer among the three equivalent <110> directions. Rotation around the center atom never occurs. Both lengthwise hopping and rotation result in a displacement of the center of mass by one Ag(111) nearest-neighbor distance, 0.289 nm, shown in the representative trajectory in (d). The rotation direction depends on chain orientation and pivot atom, with the only observed rotations depicted in the models below the images. The solid circles indicate the initial atom locations, the open circles the final locations, and the arrows indicate the directions of rotation.

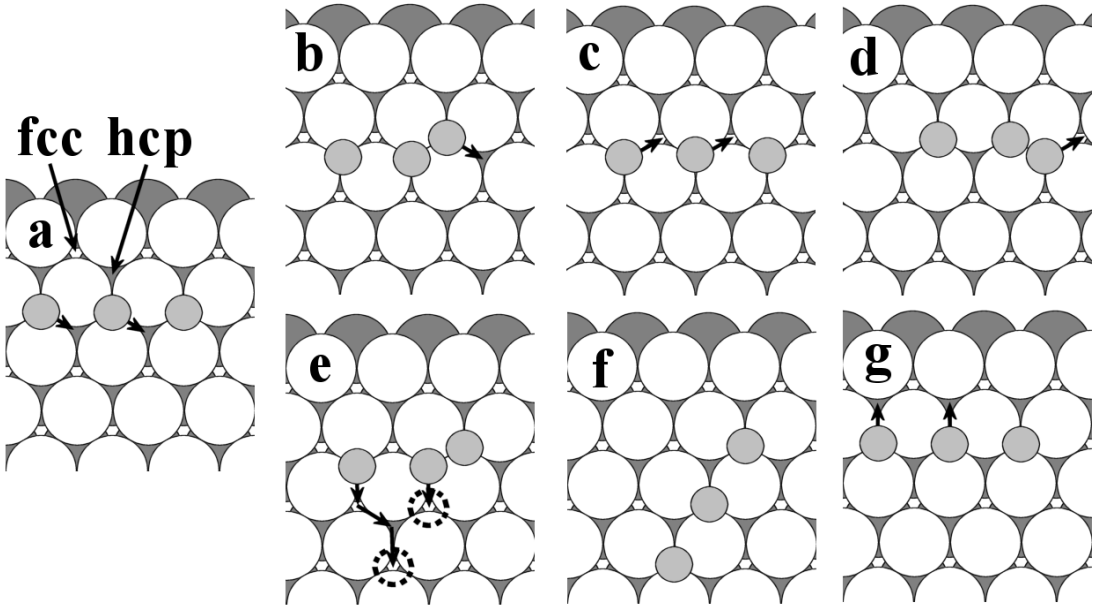

Figure 4.4 Models showing displacements that could lead to the hopping (a-d) and rotation (a,e-f) observed experimentally. With this model, rotation and hopping share a step (b, e) involving hcp sites. We argue that the lattice mismatch favors transitions from fcc-hcp that shorten Cu-Cu bonds, leading to the observed correlation between rotation direction and orientation. Rotation in the opposite direction is not allowed because this would involve fcc-hcp transitions that stretch Cu-Cu bonds (g).

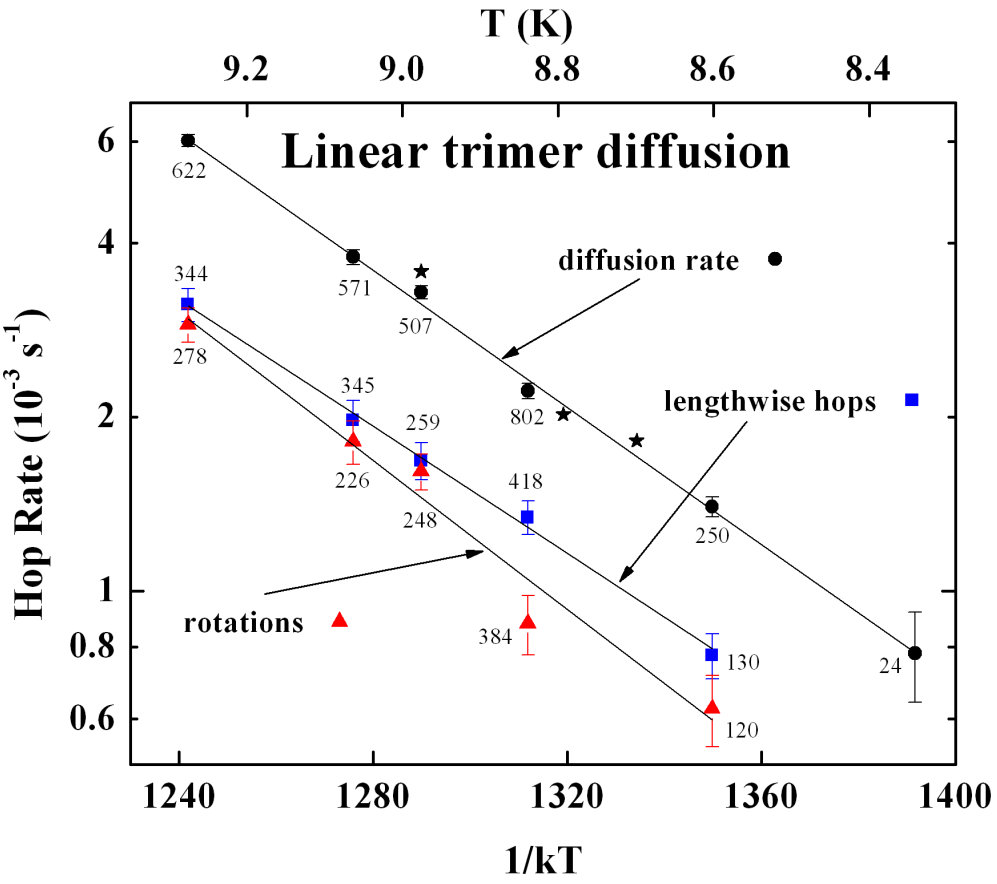

Figure 4.5 Arrhenius plot of the temperature dependence of the rates of lengthwise hopping (blue squares), rotation (red triangles), and the combined diffusion rate (black circles). Hopping and rotation occurred with statistically indistinguishable rates ($\nu_o^h = 2.1\times10^{4\pm0.5}$ s^{-1}, $E_a^h = 12.7\pm1$ meV; $\nu_o^r = 3.0\times10^{5\pm0.8}$ s^{-1}, $E_a^r = 14.8\pm1.5$ meV), leading to the same net displacement of one nearest-neighbor distance and the net diffusion rates indicated by the black circles ($\nu_o^d = 1.3\times10^{5\pm0.4}$ s^{-1}, $E_a^d = 13.6\pm0.7$ meV). The stars indicate diffusion rates measured for a second trimer chain that was constructed, indicating the reproducibility of the results.

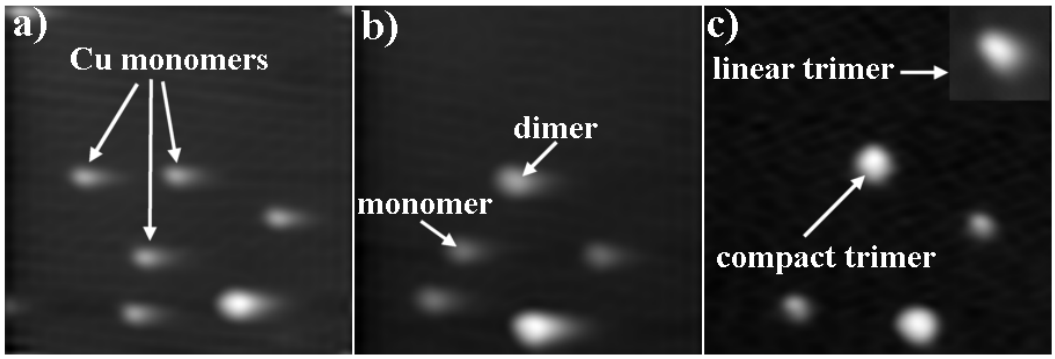

Figure 4.6 Images showing the construction of a compact trimer at 5 K. Between frames (a) and (b), a dimer was formed by moving the left-most atom into the center atom. Between frames (b) and (c), a compact trimer was formed by moving the final atom into the dimer. The inset shows a linear trimer, allowing for comparison

APPENDIX A: MATLAB PROGRAM "MATTRACK"

The following Matlab program was used to locate the coordinates of islands in each image of a data set. The original version was created by J. C. Crocker and D. G. Grier, J. Colloid Interface Sci. **179**, 298 (1996) and I modified it for my STM application.

Program MATTRACK:

```
function out=mattrack_12_512(directory,dataset,outfldr,resolution,th,n1,n2)

warning off all
for k=n1:n2


   path=strcat(directory,'\',dataset);
   filein=sprintf('%s_%04d%s',path,k,'.bmp');
   outpath=strcat(directory,'\',outfldr,'\',dataset);

   bpout=sprintf('%s_%04d%s',strcat(outpath,'_bp'),k);
   pkoutname=strcat(outpath,'_pk');
   cntoutname=strcat(outpath,'_cnt');

   % size in pixels of a 2 nm island in a 100 nm image
   sz1=((resolution/40));
   sz2=((resolution/40));
   a=double(imread(filein));
   b=bpass(a,1,10);

   pk=pkfnd(b,th,sz1);
   cnt=cntrd(b,pk,sz2);
   pkout=double([pk (k*ones(size(pk),1))]);
   cntout=double([cnt (k*ones(size(cnt),1))]);
   pkpretrack=double([pkout(:,1) resolution-pkout(:,2) pkout(:,end)]);
   cntpretrack=double([cntout(:,1) resolution-cntout(:,2) cntout(:,end)]);
   pkpretrackname=strcat(outpath,'_pkpretrack');
   cntpretrackname=strcat(outpath,'_cntpretrack');
   imwrite(uint8(b),strcat(bpout,'.bmp'));

   if (k==n1)
      save(pkoutname,'pkout','-ASCII')
      save(cntoutname,'cntout','-ASCII')
```

```
      save(strcat(pkpretrackname,'_ascii'),'pkpretrack','-ASCII')
      save(pkpretrackname,'pkpretrack')
      save(strcat(cntpretrackname,'_ascii'),'cntpretrack','-ASCII')
      save(cntpretrackname,'cntpretrack')
   else
      save(pkoutname,'pkout','-ASCII','-append')
      save(cntoutname,'cntout','-ASCII','-append')
      save(strcat(pkpretrackname,'_ascii'),'pkpretrack','-ASCII','-append')
      save(pkpretrackname,'pkpretrack','-append')
      save(strcat(cntpretrackname,'_ascii'),'cntpretrack','-ASCII','-append')
      save(cntpretrackname,'cntpretrack','-append')


   end
   number=n2-n1;
   progress=sprintf('%04d%s%04d',k-n1+1,'/',number+1)



end


function res = bpass(arr,lnoise,lobject)
%
% ; NAME:
% ;           bpass
% ; PURPOSE:
% ;           Implements a real-space bandpass filter which suppress
% ;           pixel noise and long-wavelength image variations while
% ;           retaining information of a characteristic size.
% ;
% ; CATEGORY:
% ;           Image Processing
% ; CALLING SEQUENCE:
% ;           res = bpass( image, lnoise, lobject )
% ; INPUTS:
% ;           image:  The two-dimensional array to be filtered.
% ;           lnoise: Characteristic lengthscale of noise in pixels.
% ;                 Additive noise averaged over this length should
% ;                 vanish. MAy assume any positive floating value.
% ;           lobject: A length in pixels somewhat larger than a typical
% ;                 object. Must be an odd valued integer.
% ; OUTPUTS:
% ;           res:    filtered image.
% ; PROCEDURE:
% ;           simple 'wavelet' convolution yields spatial bandpass filtering.
```

```
% ; NOTES:
% ; MODIFICATION HISTORY:
% ;           Written by David G. Grier, The University of Chicago, 2/93.
% ;           Greatly revised version DGG 5/95.
% ;           Added /field keyword JCC 12/95.
% ;           Memory optimizations and fixed normalization, DGG 8/99.
%           Converted to Matlab by D.Blair 4/2004-ish
%           Fixed some bugs with conv2 to make sure the edges are
%           removed D.B. 6/05
%           Removed inadvertent image shift ERD 6/05
%           Added threshold to output.  Now sets all pixels with
%           negative values equal to zero.  Gets rid of ringing which
%           was destroying sub-pixel accuracy, unless window size in
%           cntrd was picked perfectly.  Now centrd gets sub-pixel
%           accuracy much more robustly ERD 8/24/05
% ;
% ;     This code 'bpass.pro' is copyright 1997, John C. Crocker and
% ;     David G. Grier.  It should be considered 'freeware'- and may be
% ;     distributed freely in its original form when properly attributed.
%
%


 b = double(lnoise);
 w = round(lobject);
 N = 2*w + 1;

 % Gaussian Convolution kernel

 sm = 0:N-1;
 r = (sm - w)/(2 * b);
 gx = exp( -r.^2) / (2 * b * sqrt(pi));
 gy = gx';

 %Boxcar average kernel: background

 bx = zeros(1,N)  + 1/N;
 by = bx';
 % Do some convolutions with the matrix and our kernels

 res = arr;
 g = conv2(res,gx,'valid');
 tmpg = g;
 g = conv2(tmpg,gy,'valid');
 tmpres = res;
 res = conv2(tmpres,bx,'valid');
 tmpres = res;
```

```
 res = conv2(tmpres,by,'valid');
 tmpg= 0;
 tmpres=0;
 arr_res=zeros(size(arr));
 arr_g = zeros(size(arr));

 arr_res((lobject+1):end-lobject,(lobject+1):end-lobject) = res;
 arr_g((lobject+1):end-lobject,(lobject+1):end-lobject) = g;
 %res = arr_g-arr_res;
 res=max(arr_g-arr_res,0);


function out=pkfnd(im,th,sz)
%pkfnd:  finds local maxima in an image to pixel level accuracy.
%  this provides a rough guess of particle
%  centers to be used by cntrd.m.  Inspired by the lmx subroutine of Grier
%  and Crocker's feature.pro
% INPUTS:
% im: image to process, particle should be bright spots on dark background with little
noise
%   ofen an bandpass filtered brightfield image (fbps.m, fflt.m or bpass.m) or a nice
%   fluorescent image
% th: the minimum brightness of a pixel that might be local maxima.
%   (NOTE: Make it big and the code runs faster
%   but you might miss some particles.  Make it small and you'll get
%   everything and it'll be slow.)
% sz:  OPTIONAL if your data's noisy, (e.g. a single particle has multiple local
% maxima), then set this optional keyword to a value slightly larger than the diameter of
your blob.  if
% multiple peaks are found withing a radius of sz/2 then the code will keep
% only the brightest.  Also gets rid of all peaks within sz of boundary
%OUTPUT:  a N x 2 array containing, [row,column] coordinates of local maxima
%          out(:,1) are the x-coordinates of the maxima
%          out(:,2) are the y-coordinates of the maxima
%CREATED: Eric R. Dufresne, Yale University, Feb 4 2005
%MODIFIED: ERD, 5/2005, got rid of ind2rc.m to reduce overhead on tip by
%Dan Blair;  added sz keyword
% ERD, 6/2005: modified to work with one and zero peaks, removed automatic
% normalization of image
% ERD, 6/2005: due to popular demand, altered output to give x and y
% instead of row and column
% ERD, 8/24/2005: pkfnd now exits politely if there's nothing above
% threshold instead of crashing rudely
```

```
%find all the pixels above threshold
%im=im./max(max(im));
ind=find(im > th);
[nr,nc]=size(im);
tst=zeros(nr,nc);
n=length(ind);
if n==0
   out=[];
   display('nothing above threshold');
   return;
end
mx=[];
%convert index from find to row and column
rc=[mod(ind,nr),floor(ind/nr)+1];
for i=1:n
   r=rc(i,1);c=rc(i,2);
   %check each pixel above threshold to see if it's brighter than it's neighbors
   %  THERE'S GOT TO BE A FASTER WAY OF DOING THIS.  I'M CHECKING
SOME MULTIPLE TIMES,
   %  BUT THIS DOESN'T SEEM THAT SLOW COMPARED TO THE OTHER
ROUTINES, ANYWAY.
   if r>1 & r<nr & c>1 & c<nc
      if im(r,c)>im(r-1,c-1) & im(r,c)>im(r,c-1) & im(r,c)>im(r+1,c-1) & ...
       im(r,c)>im(r-1,c)  & im(r,c)>im(r+1,c) &   ...
       im(r,c)>im(r-1,c+1) & im(r,c)>im(r,c+1) & im(r,c)>im(r+1,c+1)
      mx=[mx,[r,c]'];
      %tst(ind(i))=im(ind(i));
      end
   end
end
%out=tst;
mx=mx';

[npks,crap]=size(mx);

%if size is specified, then get ride of pks within size of boundary
if nargin==3 & npks>0
  %throw out all pks within sz of boundary;
   ind=find(mx(:,1)>sz & mx(:,1)<(nr-sz) & mx(:,2)>sz & mx(:,2)<(nc-sz));
   mx=mx(ind,:);
end

%prevent from finding peaks within size of each other
[npks,crap]=size(mx);
if npks > 1
```

```
   %CREATE AN IMAGE WITH ONLY PEAKS
   nmx=npks;
   tmp=0.*im;
   for i=1:nmx
      tmp(mx(i,1),mx(i,2))=im(mx(i,1),mx(i,2));
   end
   %LOOK IN NEIGHBORHOOD AROUND EACH PEAK, PICK THE BRIGHTEST
   for i=1:nmx
      roi=tmp( (mx(i,1)-floor(sz/2)):(mx(i,1)+(floor(sz/2)+1)),(mx(i,2)-
floor(sz/2)):(mx(i,2)+(floor(sz/2)+1))) ;
      [mv,indi]=max(roi);
      [mv,indj]=max(mv);
      tmp( (mx(i,1)-floor(sz/2)):(mx(i,1)+(floor(sz/2)+1)),(mx(i,2)-
floor(sz/2)):(mx(i,2)+(floor(sz/2)+1)))=0;
      tmp(mx(i,1)-floor(sz/2)+indi(indj)-1,mx(i,2)-floor(sz/2)+indj-1)=mv;
   end
   ind=find(tmp>0);
   mx=[mod(ind,nr),floor(ind/nr)+1];
end

out(:,2)=mx(:,1);
out(:,1)=mx(:,2);


function out=cntrd(im,mx,sz,interactive)
%cntrd:  calculates the centroid of bright spots to sub-pixel accuracy.
%  Inspired by Grier & Crocker's feature for IDL, but greatly simplified and optimized
%  for matlab
% INPUTS:
% im: image to process, particle should be bright spots on dark background with little
noise
%   ofen an bandpass filtered brightfield image or a nice fluorescent image
%
% mx: locations of local maxima to pixel-level accuracy from pkfnd.m
%
% sz: diamter of the window over which to average to calculate the centroid.
%     should be big enough
%     to capture the whole particle but not so big that it captures others.
%     if initial guess of center (from pkfnd) is far from the centroid, the
%     window will need to be larger than the particle size.  RECCOMMENDED
%     size is the long lengthscale used in bpass plus 2.
%
%
% interactive:  OPTIONAL INPUT set this variable to one and it will show you the
image used to calculate
%    each centroid, the pixel-level peak and the centroid
```

```
%
% NOTE:
%  - if pkfnd, and cntrd return more then one location per particle then
%  you should try to filter your input more carefully.  If you still get
%  more than one peak for particle, use the optional sz parameter in pkfnd
%  - If you want sub-pixel accuracy, you need to have a lot of pixels in your window
(sz>>1).
%    To check for pixel bias, plot a histogram of the fractional parts of the resulting
locations
%  - It is HIGHLY recommended to run in interactive mode to adjust the parameters
before you
%    analyze a bunch of images.
%
%OUTPUT:  a N x 3 array containing, x, y and brightness for each feature
%          out(:,1) is the x-coordinates
%          out(:,2) is the y-coordinates
%          out(:,3) is the brightnesses
%          out(:,4) is the sqare of the radius of gyration
%
%CREATED: Eric R. Dufresne, Yale University, Feb 4 2005
%  5/2005 inputs diamter instead of radius
%  Modifications:
%  D.B. (6/05) Added code from imdist/dist to make this stand alone.
%  ERD (6/05) Increased frame of reject locations around edge to 1.5*sz
%  ERD 6/2005  By popular demand, 1. altered input to be formatted in x,y
%  space instead of row, column space  2. added forth column of output,
%  rg^2
%  ERD 8/05  Outputs had been shifted by [0.5,0.5] pixels.  No more!
%  ERD 8/24/05  Woops!  That last one was a red herring.  The real problem
%  is the "ringing" from the output of bpass.  I fixed bpass (see note),
%  and no longer need this kludge.  Also, made it quite nice if mx=[];


if nargin==3
  interactive=0;
end

if sz/2 == floor(sz/2)
warning('sz must be odd, like bpass');
end

if isempty(mx)
   warning('there were no positions inputted into cntrd. check your pkfnd theshold')
   out=[];
   return;
end
```

```
r=(sz+1)/2;
%create mask - window around trial location over which to calculate the centroid
m = 2*r;
x = 0:(m-1) ;
cent = (m-1)/2;
x2 = (x-cent).^2;
dst=zeros(m,m);
for i=1:m
   dst(i,:)=sqrt((i-1-cent)^2+x2);
end


ind=find(dst < r);

msk=zeros([2*r,2*r]);
msk(ind)=1.0;
%msk=circshift(msk,[-r,-r]);

dst2=msk.*(dst.^2);
ndst2=sum(sum(dst2));

[nr,nc]=size(im);
%remove all potential locations within distance sz from edges of image
ind=find(mx(:,2) > 1.5*sz & mx(:,2) < nr-1.5*sz);
mx=mx(ind,:);
ind=find(mx(:,1) > 1.5*sz & mx(:,1) < nc-1.5*sz);
mx=mx(ind,:);

[nmx,crap] = size(mx);

%inside of the window, assign an x and y coordinate for each pixel
xl=zeros(2*r,2*r);
for i=1:2*r
   xl(i,:)=(1:2*r);
end
yl=xl';

pts=[];
%loop through all of the candidate positions
for i=1:nmx
   %create a small working array around each candidate location, and apply the window
function
   tmp=msk.*im((mx(i,2)-r+1:mx(i,2)+r),(mx(i,1)-r+1:mx(i,1)+r));
   %calculate the total brightness
```

```
    norm=sum(sum(tmp));
    %calculate the weigthed average x location
    xavg=sum(sum(tmp.*xl))./norm;
    %calculate the weighted average y location
    yavg=sum(sum(tmp.*yl))./norm;
    %calculate the radius of gyration^2
    rg=(sum(sum(tmp.*dst2))/ndst2);

    %concatenate it up
    pts=[pts,[mx(i,1)+xavg-r,mx(i,2)+yavg-r,norm,rg]'];

    %OPTIONAL plot things up if you're in interactive mode
    if interactive==1
     imagesc(tmp)
     axis image
     hold on;
     plot(xavg,yavg,'x')
     plot(xavg,yavg,'o')
     plot(r,r,'.')
     hold off
     pause
    end


end
out=pts';
```

APPENDIX B: MATLAB PROGRAM "TRAJ"

The program "Mattrack", presented in Appendix A, creates a list of coordinates for islands in each image of a data set. In order to build particle trajectories, those coordinates must be correlated over time. The Matlab code used for that procedure was created by Professor Eric Weeks' research group and can be found and freely downloaded at http://www.physics.emory.edu/~weeks/idl/. Because the code is very lengthy and was used in its unmodified form, it will not be presented here. The output of that tracking program is four columns of data: x, y, image frame, particle number. The trajectories created by this program are not calibrated and contain experimental artifacts, such as thermal drift of the microscope. In order to correct for drift and calibrate the units of measurement, I wrote the following program. To correct for drift, trajectories of immobile features on the surface were subtracted from the ones to be tracked, creating accurate and atomically-precise trajectories for each particle.

Program TRAJ:

```
function Traj12(directory,dataset,outfldr,first,last)
tic
warning off all
track=load(strcat(directory,'\',dataset,'_track'));
immobile=load(strcat(directory,'\',dataset,'_immobile.txt'));
cal=load(strcat(directory,'\',dataset,'_cal.txt'));
extractsize=max(track(:,4));
extract=zeros(max(track(:,4)),2);

for k=first:last %min(track(:,4)):max(track(:,4))
```

```
f=1;
s=1;
[r,c,v]=find(track(:,4)==k);
Tra=track(r,:);
Trasize=size(Tra,1);
Trasize;


ydiff=5000;
yimm=0;

for m=1:size(immobile,1)
   immobile(m);
   [r,c,v]=find(track(:,4)==immobile(m));
   r;
   ref=track(r,:);
   [r,c,v]=find(ref(:,3)==Tra(1,3));
    if (min(ref(:,3))>min(Tra(:,3))||max(ref(:,3))<max(Tra(:,3))||immobile(m)==k)
      continue
   end
   yimm=ref(r,2);

   if ydiff>=abs(Tra(1,2)-ref(r,2))%&&(size(ref,1)>=size(Tra,1))
      Ref=ref;
      ydiff=abs(Tra(1,2)-Ref(r,2));
      extract(k,1)=Tra(1,4);
      extract(k,2)=immobile(m);
      extract;
   end
   yimm;
      ydiff;
      abs(Tra(1,2));
      %size(Ref,1)
      %size(Tra,1)
      %Ref;
      %Tra;
end


%[r,c,v]=find(track(:,4)==extract(k,2));
%Ref=track(r,:);
%need the following 2 lines, in case Tra and Ref begin on different
%frames
[r,c,v]=find(Tra(1,3)<=Ref(:,3) & Ref(:,3)<=Tra(Trasize,3));
r;
Ref=Ref(r,:);
```

```
    Tra;
    %need to insert dummy line if particle lost for a frame
    %[r,c,v]=find(Tra(:,3)~=
    %Refsize=size(Ref,1)
    %size(Tra)
    %size(Ref)
    %(1)Frame (2)Time (3)zeros (4)zeros (5)zeros (6)x-pix (7)y-pix (8)x-nm,
    %DC (9)y-nm, DC (10)zeros (11)zeros
    a=Tra(:,1:2);
    Tra=[Tra(:,3) (Tra(:,3)-Tra(1,3))*cal(5)*cal(4)*2/cal(6)...
    zeros(size(Tra,1),1) zeros(size(Tra,1),1) zeros(size(Tra,1),1)...
    Tra(:,1) Tra(:,2) (Tra(:,1)-Tra(1,1)-Ref(:,1)+Ref(1,1))*cal(1)*cal(5)/cal(3)...
    (Tra(:,2)-Tra(1,2)-Ref(:,2)+Ref(1,2))*cal(2)*cal(5)/cal(3)...
    zeros(size(Tra,1),1) zeros(size(Tra,1),1)];
    %Tra(:,8:9)
    %Ref(:,1:2)
    %b=[a Ref(:,1:2) Tra(:,8:9)]

    %tcal time, taking into account (x,y) position and scan rate
    Tra(:,4)=Tra(:,2)+((cal(5)/(cal(6)*cal(3))*(Tra(:,6)+2*cal(4)*Tra(:,7))));
    %delta t time between images
    Tra(:,3)=Tra(:,2)-circshift(Tra(:,2),1);
    %delta tcal, change in tcal between images
    Tra(:,5)=Tra(:,4)-circshift(Tra(:,4),1);
    %Tra(:,10)=((Tra(:,8)-circshift(Tra(:,8),1))^2+(Tra(:,9)-
circshift(Tra(:,9),1))^2)/(Tra(:,3)*2);

    for j=2:Trasize
        %squared displacement nm^2
        Tra(j,10)=((Tra(j,8)-Tra(j-1,8))^2+(Tra(j,9)-Tra(j-1,9))^2);
        %mean squared displacement (running average of squared
        %displacement) nm^2
        Tra(j,11)=sum(Tra(1:j,10))/(j-1);
        %SD/4deltat nm^2/sec
        Tra(j,12)=((Tra(j,8)-Tra(j-1,8))^2+(Tra(j,9)-Tra(j-1,9))^2)/(4*Tra(j,3));
        %MSD/4t nm^2/sec
        Tra(j,13)=sum(Tra(1:j,12))/(j-1);
        %SD/4deltatcal nm^2/sec
        Tra(j,14)=((Tra(j,8)-Tra(j-1,8))^2+(Tra(j,9)-Tra(j-1,9))^2)/(4*Tra(j,5));
        %MSD/4deltatcal nm^2/sec
        Tra(j,15)=sum(Tra(1:j,14))/(j-1);
        %r distance from (0,0) in nm
        Tra(j,16)=sqrt(Tra(j,8)^2+Tra(j,9)^2);
        %deltar hop length between images
        Tra(j,17)=sqrt(Tra(j,10));
        Tra(1,18)=0;
```

```
    Tra(1,19)=0;

    %Tra(:,18)=flight IDs  Tra(:,19)=stick IDs
    if Tra(j,17)>=0.1
       if (Tra(j-1,19)>0)&&(Tra(j-1,19)~=1)
       f=f+1;
       end
       Tra(j,18)=f;
    else
       if Tra(j-1,18)>0
          s=s+1;
       end
       Tra(j,19)=s;
    end

  %Save "extract", the list of mobile and reference island pairs
  x=[extract(find(extract(:,1)),1) extract(find(extract(:,2)),2)];
  save(strcat(directory,'\',outfldr,'\',dataset,'_extract'),'x','-ASCII')
  end

  %Save the matrix of processed data
  save(strcat(directory,'\',outfldr,'\',dataset,'_',sprintf('%05g',extract(k,1)),'_traj1'),'Tra','-
ASCII')



  %Plot the drift-corrected, calibrated x-y trajectory  and save it as a
  %jpg.
  plot(Tra(:,8),Tra(:,9),'- ok','MarkerFaceColor', 'k','MarkerSize',2)
  axis([-int8(max([max(abs(Tra(:,8))) max(abs(Tra(:,9)))])+1)
int8(max([max(abs(Tra(:,8))) max(abs(Tra(:,9)))])+1) -int8(max([max(abs(Tra(:,8)))
max(abs(Tra(:,9)))])+1) int8(max([max(abs(Tra(:,8))) max(abs(Tra(:,9)))])+1)])
  axis square
  grid on
  title(sprintf('%s%05g',strcat(dataset(1:6),'--',dataset(8:10),'--'),extract(k,1)))
  xlabel('x (nm)')
  ylabel('y (nm)')
  saveas(1,strcat(directory,'\',outfldr,'\',dataset,'_',sprintf('%05g',extract(k,1)),'_xy'),'jpg')
  %save(strcat(directory,'\',outfldr,'\',dataset,'_plot',extract(k,1)),'1','-ASCII')

  %Plot the mean-square-displacement of the island as a function of movie
  %frame and save it as a jpg.
  plot(Tra(:,1),Tra(:,11),'-k')
  title(sprintf('%s%05g',strcat(dataset(1:6),'--',dataset(8:10),'--'),extract(k,1)))
  xlabel('Frame')
  ylabel('<\Deltax^2> (nm^2)')
```

```
saveas(1,strcat(directory,'\',outfldr,'\',dataset,'_',sprintf('%05g',extract(k,1)),'_MSD'),'jpg')

%saveas(1,sprintf('%s%05g',strcat(directory,'\',outfldr,'\',dataset,'_MSD_'),extract(k,1)),'j
pg')


   %plot x vs frame # and save a jpg
   plot(Tra(:,1),Tra(:,8),'-k')
   title(sprintf('%s%05g',strcat(dataset(1:6),'--',dataset(8:10),'--'),extract(k,1)))
   xlabel('Frame')
   ylabel('x (nm)')

saveas(1,strcat(directory,'\',outfldr,'\',dataset,'_',sprintf('%05g',extract(k,1)),'_xtime'),'jpg')

   %plot y vs frame # and save a jpg
   plot(Tra(:,1),Tra(:,9),'-k')
   title(sprintf('%s%05g',strcat(dataset(1:6),'--',dataset(8:10),'--'),extract(k,1)))
   xlabel('Frame')
   ylabel('y (nm)')

saveas(1,strcat(directory,'\',outfldr,'\',dataset,'_',sprintf('%05g',extract(k,1)),'_ytime'),'jpg')



%saveas(1,sprintf('%s%05g',strcat(directory,'\',outfldr,'\',dataset,'_MSD_'),extract(k,1)),'j
pg')
  %plot the island distance from the origin, "r", vs frame # and save a jpg
   plot(Tra(:,1),Tra(:,16),'-k')
   title(sprintf('%s%05g',strcat(dataset(1:6),'--',dataset(8:10),'--'),extract(k,1)))
   xlabel('Frame')
   ylabel('r (nm)')

saveas(1,strcat(directory,'\',outfldr,'\',dataset,'_',sprintf('%05g',extract(k,1)),'_rtime'),'jpg')

   %histogram of hop displacements, saved as a separate matrix "lhist",
   %and plotted as a jpg
   x=0:.0289:2.89;
   [n,xout]=hist(Tra(:,17),x);
   save(strcat(directory,'\',outfldr,'\',dataset,'_',sprintf('%05g',extract(k,1)),'_lhist'),'n','-
ASCII')
   plot(xout,n,'- ok','MarkerFaceColor', 'k','MarkerSize',2)
   title(sprintf('%s%05g',strcat(dataset(1:6),'--',dataset(8:10),'--'),extract(k,1)))
   xlabel('Displacement (nm)')
   ylabel('# Hops')
```

```
saveas(1,strcat(directory,'\',outfldr,'\',dataset,'_',sprintf('%05g',extract(k,1)),'_lhist'),'jpg')

   %histogram of squared hop lengths, saved as a separate matrix,
   %"l2hist", and plotted as a jpg

   x=0:0.0083521:8.3521/10;
   [n,xout]=hist(Tra(:,10),x);
   save(strcat(directory,'\',outfldr,'\',dataset,'_',sprintf('%05g',extract(k,1)),'_l2hist'),'n','-
ASCII')
   plot(xout,n,'- ok','MarkerFaceColor', 'k','MarkerSize',2)
   title(sprintf('%s%05g',strcat(dataset(1:6),'--',dataset(8:10),'--'),extract(k,1)))
   xlabel('Squared Displacement (nm)')
   ylabel('# Hops')

saveas(1,strcat(directory,'\',outfldr,'\',dataset,'_',sprintf('%05g',extract(k,1)),'_l2hist'),'jpg')




   progress=sprintf('%03d%s%03d',k-first+1,'/',last-first+1)
   toc

   %subroutine to extract flight and stick times and distances
   flight=zeros(max(Tra(:,18)),3);
for l=1:max(Tra(:,18))
[r,c,v]=find(Tra(:,18)==l);
flight(l,1)=l;
flight(l,2)=size(r,1)*Tra(r(1),5);
flight(l,3)=sum(Tra(r(1):r(size(r,1)),17));
end


%Save the matrix of flight and stick data
save(strcat(directory,'\',outfldr,'\',dataset,'_',sprintf('%05g',extract(k,1)),'_flight'),'flight','-
ASCII')

%plot the flight distance vs flight time
plot(flight(:,2),flight(:,3),'ok','MarkerFaceColor', 'k','MarkerSize',2)
title(sprintf('%s%05g',strcat(dataset(1:6),'--',dataset(8:10),'--'),extract(k,1)))
xlabel('Flight Time (sec)')
ylabel('Flight Distance (nm)')

%save the plot as a jpeg
%NOTE: if there are no flights (the island didn't move by more than
```

```
%the "Flight" cutoff distance, then the above plot command will do nothing,
%but the title and axes labels will simply change the labels.
saveas(1,strcat(directory,'\',outfldr,'\',dataset,'_',sprintf('%05g',extract(k,1)),'_flight'),'jpg')

end




end
```

AUTHOR'S BIOGRAPHY

Andrew William Signor earned his Bachelor's of Science in Materials Science and Engineering from Virginia Polytechnic Institute and State University (Virginia Tech) in 2002. During his undergraduate work, he was employed as a co-op student researcher at the National Institute of Standards and Technology, where he investigated the effects of ultra-violet radiation on the mechanical and thermal properties of fiber-reinforced polymer composites. Following the completion of his Ph.D., A. W. Signor will begin work for CREE, in Durham, NC, as a Research Scientist.